

## RESEARCH ARTICLE

# Delayed global feedback in the genesis and stability of spatiotemporal excitation patterns in paced biological excitable media

Zhen Song<sup>1,2\*</sup>, Zhilin Qu<sup>1,3\*</sup>

**1** Department of Medicine, David Geffen School of Medicine, University of California Los Angeles, Los Angeles, California, United States of America, **2** Peng Cheng Laboratory, Shenzhen, China, **3** Department of Computational Medicine, David Geffen School of Medicine, University of California Los Angeles, Los Angeles, California, United States of America

\* [songzh01@pcl.ac.cn](mailto:songzh01@pcl.ac.cn) (ZS); [zqu@mednet.ucla.edu](mailto:zqu@mednet.ucla.edu) (ZQ)



## OPEN ACCESS

**Citation:** Song Z, Qu Z (2020) Delayed global feedback in the genesis and stability of spatiotemporal excitation patterns in paced biological excitable media. *PLoS Comput Biol* 16(10): e1007931. <https://doi.org/10.1371/journal.pcbi.1007931>

**Editor:** Andrew D. McCulloch, University of California San Diego, UNITED STATES

**Received:** May 1, 2020

**Accepted:** July 22, 2020

**Published:** October 5, 2020

**Copyright:** © 2020 Song, Qu. This is an open access article distributed under the terms of the [Creative Commons Attribution License](https://creativecommons.org/licenses/by/4.0/), which permits unrestricted use, distribution, and reproduction in any medium, provided the original author and source are credited.

**Data Availability Statement:** All relevant data are within the manuscript and its Supporting Information files.

**Funding:** Z.Q. received the grant from National Institutes of Health R01 HL134709 and R01 HL133294 (<https://www.nih.gov/grants-funding>). The funders had no role in study design, data collection and analysis, decision to publish, or preparation of the manuscript.

**Competing interests:** The authors have declared that no competing interests exist.

## Abstract

Biological excitable media, such as cardiac or neural cells and tissue, exhibit memory in which a change in the present excitation may affect the behaviors in the next excitation. For example, a change in calcium ( $\text{Ca}^{2+}$ ) concentration in a cell in the present excitation may affect the  $\text{Ca}^{2+}$  dynamics in the next excitation via bi-directional coupling between voltage and  $\text{Ca}^{2+}$ , forming a delayed feedback loop. Since the  $\text{Ca}^{2+}$  dynamics inside the excitable cells are spatiotemporal while the membrane voltage is a global signal, the feedback loop is then a delayed global feedback (DGF) loop. In this study, we investigate the roles of DGF in the genesis and stability of spatiotemporal excitation patterns in periodically-paced excitable media using mathematical models with different levels of complexity: a model composed of coupled FitzHugh-Nagumo units, a 3-dimensional physiologically-detailed ventricular myocyte model, and a coupled map lattice model. We investigate the dynamics of excitation patterns that are temporal period-2 (P2) and spatially concordant or discordant, such as subcellular concordant or discordant  $\text{Ca}^{2+}$  alternans in cardiac myocytes or spatially concordant or discordant  $\text{Ca}^{2+}$  and repolarization alternans in cardiac tissue. Our modeling approach allows both computer simulations and rigorous analytical treatments, which lead to the following results and conclusions. When DGF is absent, concordant and discordant P2 patterns occur depending on initial conditions with the discordant P2 patterns being spatially random. When the DGF is negative, only concordant P2 patterns exist. When the DGF is positive, both concordant and discordant P2 patterns can occur. The discordant P2 patterns are still spatially random, but they satisfy that the global signal exhibits a temporal period-1 behavior. The theoretical analyses of the coupled map lattice model reveal the underlying instabilities and bifurcations for the genesis, selection, and stability of spatiotemporal excitation patterns.

## Author summary

Understanding the mechanisms of pattern formation in biological systems is of great importance. Here we investigate the dynamical mechanisms by which delayed global feedback affects excitation pattern formation and stability in periodically-paced biological excitable media, such as cardiac or neural cells and tissue. We focus on the formation and stability of the temporal period-2 and spatially in-phase and out-of-phase excitation patterns. Using models of different levels of complexity, we show that when the delayed global feedback is negative, only the spatially in-phase patterns are stable. When the feedback is positive, both spatially in-phase and out-of-phase patterns are stable, and the out-of-phase patterns are spatially random but satisfy that the global signals are temporal period-1 solutions.

## Introduction

Pattern formation is ubiquitous in biological systems, ranging from biological development [1, 2], ecosystems [3], to disease development [4]. Many of the pattern formation processes can be explained by Turing instability in reaction-diffusion (or activator-inhibitor) systems [5, 6]. However, pattern formation via other mechanisms has also been proposed, in particular for spatiotemporal patterns, which are also widely observed in biological systems [7–12]. The fundamental processes causing temporal and spatiotemporal dynamics in biological systems are positive and negative feedback loops [5, 6, 13]. While many studies investigated the roles of local and instantaneous feedback loops in pattern formation, studies have also carried out to investigate the roles of instantaneous global feedback and time delay global feedback (DGF) loops, such as the ones demonstrated in oscillatory media of chemical reactions [14–19]. In this study, we focus on the roles of DGF in excitation pattern formation in a class of biological systems, i.e., excitable media subjected to periodic global stimulation. Examples of pattern formation in such biological systems include subcellular calcium ( $\text{Ca}^{2+}$ ) release patterns in neural or cardiac cells (see examples in [S1 Fig](#)) or repolarization (voltage) patterns in cardiac tissue or cluster firings in neural networks, as described in more detail below.

In the chemical reaction experiments [17, 19], the DGF loops were explicitly implemented. However, the DGF loops are not obvious at all in the excitable biological systems. Here we use intracellular  $\text{Ca}^{2+}$  signaling, which is required for many biological functions [20, 21], as an example to explain the existence of DGF. The fundamental unit of  $\text{Ca}^{2+}$  signaling in a cell is called  $\text{Ca}^{2+}$  release unit (CRU) ([Fig 1A](#)).  $\text{Ca}^{2+}$  entering the cell from the voltage-gated  $\text{Ca}^{2+}$  channels triggers the opening of the  $\text{Ca}^{2+}$  release channels to release  $\text{Ca}^{2+}$  from the internal  $\text{Ca}^{2+}$  stores. The open probability of the  $\text{Ca}^{2+}$  release channels is further enhanced by the released  $\text{Ca}^{2+}$ . This process is known as  $\text{Ca}^{2+}$ -induced  $\text{Ca}^{2+}$  release (CICR), which is an instantaneous local feedback loop responsible for a rich spectrum of  $\text{Ca}^{2+}$  dynamics widely observed in biological systems [22–26]. Besides this instantaneous feedback loop, implicit delayed feedback loops exist, i.e.,  $\text{Ca}^{2+}$  in the present beat may affect itself in the next beat ([Fig 1B](#)). This feedback can be mediated by the  $\text{Ca}^{2+}$  current ( $I_{\text{Ca}}$ ) of the voltage-gated  $\text{Ca}^{2+}$  channels or the  $\text{Ca}^{2+}$  release properties of the internal stores through either voltage or  $\text{Ca}^{2+}$ -dependent signaling pathways. For example, in cardiac myocytes,  $\text{Ca}^{2+}$  is coupled to voltage via  $\text{Ca}^{2+}$ -dependent ion channels and pumps. Changing  $\text{Ca}^{2+}$  in the present beat changes the action potential (AP) duration (APD) and thus the following diastolic interval (DI), affecting the recovery of voltage-gated  $\text{Ca}^{2+}$  channels in the next beat. As a result, the change in the recovery alters  $I_{\text{Ca}}$  and hence  $\text{Ca}^{2+}$ , forming a delayed feedback loop. Note that in excitable cells, ion channels

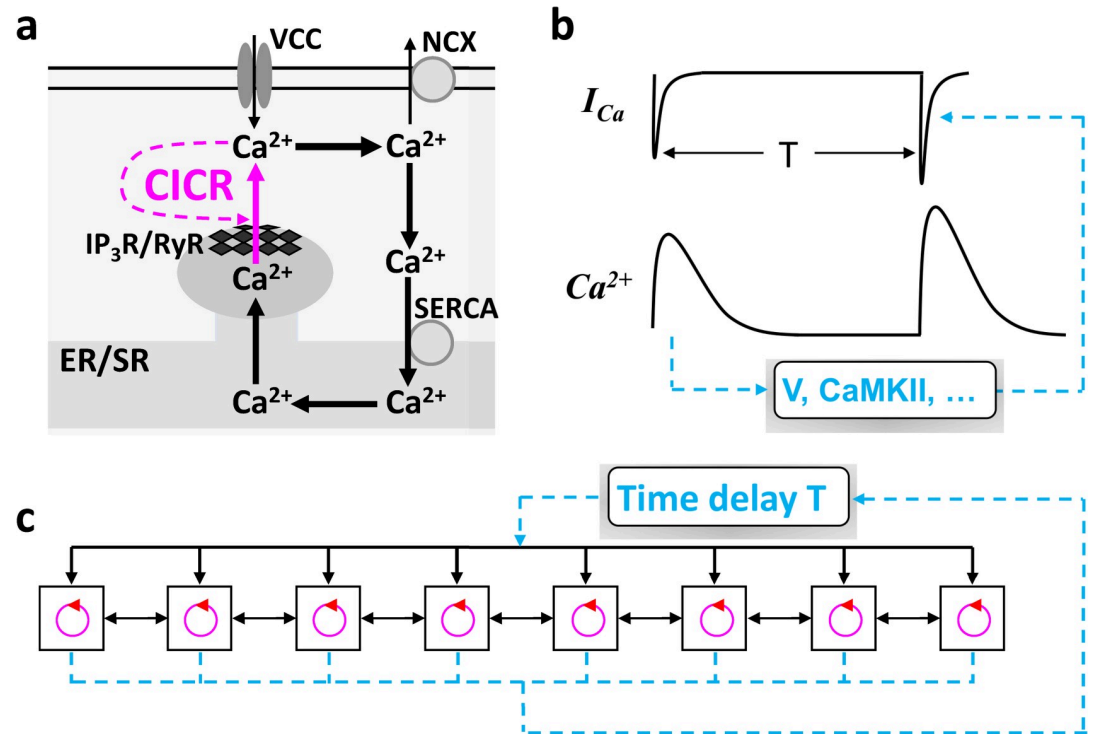


**Fig 1. Schematic diagrams of Ca<sup>2+</sup> cycling and a generic model of coupled excitable units with DGF.** **a.** Schematic diagram of a basic Ca<sup>2+</sup> release unit (CRU) in excitable cells. Ca<sup>2+</sup> from voltage gated Ca<sup>2+</sup> channels (VCCs) triggers the opening of the inositol trisphosphate receptors (IP3Rs) or ryanodine receptors (RyRs), releasing the Ca<sup>2+</sup> stored in the endoplasmic or sarcoplasmic reticulum (ER/SR). The released Ca<sup>2+</sup> further triggers more IP3Rs/RyRs to open, forming a positive feedback loop. This process is called Ca<sup>2+</sup>-induced Ca<sup>2+</sup> release (CICR). Ca<sup>2+</sup> is extruded by Na<sup>+</sup>-Ca<sup>2+</sup> exchange (NCX) or other Ca<sup>2+</sup> pumps and uptaken back into the ER/SR via sarco/endoplasmic reticulum Ca<sup>2+</sup> ATPase (SERCA). **b.** Schematic diagram of delayed feedback in Ca<sup>2+</sup> signaling via Ca<sup>2+</sup> current (I<sub>Ca</sub>). T is the pacing period. **c.** Schematic diagram of a generic model of coupled excitable units (e.g., CRUs) with a DGF loop of time delay T.

<https://doi.org/10.1371/journal.pcbi.1007931.g001>

generally remain in closed or inactivation states in the quiescent phase. Therefore, the effects of this delayed feedback are manifested in the next beat. In other words, the time delay of the feedback loop is simply the pacing period T.

A cell consists of thousands of CRUs which are coupled via Ca<sup>2+</sup> diffusion. The CRUs are themselves excitable units [24, 27–29], which are triggered by a global signal, i.e., voltage. Therefore, one can simplify the Ca<sup>2+</sup> signaling system into a coupled array of excitable units under a global stimulation with a DGF loop (Fig 1C). Since voltage is the global signal, under normal conditions, depolarization of the cell synchronizes the firings of the CRUs, resulting in a synchronous whole-cell Ca<sup>2+</sup> release, such as Ca<sup>2+</sup> release in neurons (S1A Fig) [30]. The synchronous Ca<sup>2+</sup> release is essential for muscle contraction [21] and many other types of biological functions [20]. However, under abnormal or diseased conditions, dyssynchronous Ca<sup>2+</sup> releases can occur, such as subcellular spatially discordant Ca<sup>2+</sup> alternans widely observed in cardiac myocytes (S1B Fig) [31–33]. It is clear that voltage serves as the global signal to synchronize the CRU releases, but it is unclear how dyssynchronous or discordant patterns are formed. Furthermore, the roles of the DGF in maintaining the synchronous release patterns or the development of the dyssynchronous release patterns are not well understood.

In addition to intracellular Ca<sup>2+</sup> signaling, other biological systems can also be described by the simplified scheme in Fig 1C, such as the excitation dynamics in cardiac tissue or neural networks. In cardiac tissue, myocytes are electrically excitable units that are coupled via gap

junctions. Contraction of the heart can serve as the global signal, which may mediate DGF via mechano-electric feedback through activating mechano-sensitive channels and affecting intracellular  $\text{Ca}^{2+}$  release [34–36]. This DGF may play essential roles in arrhythmogenic pattern formation in the heart, such as the widely observed spatially discordant APD alternans [37, 38]. In neural networks, the roles of delayed feedback in neural firing dynamics have been investigated [39–41], and DGF may also play essential roles in the formation and stability of clustered firing of neurons [42].

This study was set to investigate the roles of DGF in the genesis and stability of spatiotemporal patterns in periodically-paced biological excitable media, focusing on temporal period-2 (P2) and spatially concordant (in-phase) or discordant (out-of-phase) patterns. Mathematical models of different levels of complexity were used to allow both computer simulations and rigorous analytical treatments. First, a generic model consisting of a coupled array of excitable units described by the FitzHugh-Nagumo (FHN) model was used, and simulations were carried out to reveal the pattern dynamics caused by DGF. To validate the findings of the generic model, we used a 3-dimensional (3D) ventricular myocyte model and carried out simulations to investigate the roles of DGF in spatially concordant and discordant  $\text{Ca}^{2+}$  alternans dynamics. Of note, the term “alternans” in the context of the cardiac systems refers to a P2 state. Finally, a coupled map lattice (CML) model was used to perform detailed theoretical analyses, which provide a general mechanistic understanding of the roles of DGF in pattern formation, selection, and stability in periodically-paced biological excitable media. Our approach or objective is to use the generic FHN model to demonstrate that the DGF induced dynamics are general, use the detailed ventricular cell model to validate the general dynamics in a realistic biological system, and use the CML model to reveal the underlying dynamical mechanisms. We argue (as detailed in Discussion) that besides the subcellular spatiotemporal  $\text{Ca}^{2+}$  dynamics in ventricular myocytes, due to the generality of the simple models, the mechanistic insights shall also be applicable to spatially discordant APD alternans in cardiac tissue or cluster firings in neural networks when global feedback or DGF exists. The theoretical insights may also be helpful for understanding the mechanisms of pattern formation induced by global feedback or DGF in oscillatory chemical media shown in previous studies [14–19].

## Results

### DGF in the genesis of spatiotemporal dynamics in an array of coupled FHN units

We used a generic model consisting of a one-dimensional (1D) array of coupled FHN units to investigate the spatiotemporal excitation patterns. The governing differential equations are:

$$\begin{aligned} \frac{dc(j, t)}{dt} &= f[c(j, t), w(j, t)] + D[c(j+1, t) + c(j-1, t) - 2c(j, t)] + I(t) \\ \frac{dw(j, t)}{dt} &= g[c(j, t), w(j, t)] \end{aligned} \quad (1)$$

in which  $j = 1, 2, \dots, L$  is the spatial index of the FHN units with  $L$  being the length of the 1D array. We used the standard FHN kinetics, i.e.,

$$f(c, w) = -c(c-1)(c-c_{th}) - 0.1w, g(c, w) = (c - 0.25w - 0.3)/10 \quad (2)$$

where  $c$  is the activator and  $w$  the inhibitor.  $c_{th} = 0.5$  is a parameter determining the threshold

for excitation, and  $D = 0.1$  is the coupling strength.  $I(t)$  in Eq 1 is the external stimulus pulse. No-flux boundary condition was used.

As implied in Fig 1B,  $I_{Ca}$  that triggers the  $Ca^{2+}$  release and mediates the feedback is a spiky current, which only occurs at the beginning of each pacing beat. Therefore, instead of adding a time-continuous feedback term to Eq 1, we add the feedback to the stimulus pulse, which is then formulated as

$$I(t) = \begin{cases} I_0[1 + \alpha(\bar{c}_{n-1} - \bar{c}_s)], & \text{if } nT < t < nT + \Delta T \\ 0, & \text{otherwise} \end{cases} \quad (3)$$

In Eq 3,  $n$  is the index of the beat number,  $T$  is the pacing period,  $\Delta T$  is the pulse duration, and  $\alpha$  is the feedback strength.  $\bar{c}_{n-1}$  is the peak value of the spatial average of  $c$  (denoted as  $\bar{c}(t)$ ) at the  $(n-1)^{\text{th}}$  beat.  $\bar{c}_s$  is the reference value for the feedback. Here we define  $\alpha > 0$  as positive feedback ( $\alpha < 0$  as negative feedback), since in an uncoupled FHN unit, a larger  $c_{n-1}$  gives rise to a larger  $I(t)$ , and thus a larger  $c_n$ . We set  $I_0 = 1.2$ ,  $\Delta T = 0.5$ , and  $\bar{c}_s = 0.77$ . The  $\bar{c}_s$  value is roughly the steady-state value of  $c$  at the bifurcation point from P1 to P2 of an FHN unit without feedback. We find that other choices do not change the general results but exhibit certain quantitative differences.

Random initial conditions are used to induce spatially discordant patterns. Specifically, at  $t = 0$ , we set the variable  $w$  to be a spatially random distribution, i.e.,  $w(j,0) = 0.5 + \delta \xi(j)$  ( $j = 1, 2, \dots, L$ ) with  $\xi(j)$  being a uniform random number in  $[-1, 1]$ .  $\delta$  is the parameter determining the extent of the spatial heterogeneity and the initial condition becomes uniform when  $\delta = 0$ .

**Excitation patterns without DGF.** In the absence of DGF, i.e.,  $\alpha = 0$  in Eq 3, a bifurcation from temporal P1 to P2 occurs as the pacing period  $T$  decreases in an uncoupled FHN unit (S2 Fig). We use spatially random initial conditions as detailed above to induce discordant patterns in the 1D array. We find that when  $T$  first passes through the bifurcation point, the system can only exhibit a spatially concordant P2 (Con-P2) pattern independent of initial conditions. As  $T$  decreases further, the system can exhibit a Con-P2 (Fig 2A) or a spatially discordant P2 (Dis-P2) pattern (Fig 2B) depending on the initial condition. The probability of forming a Dis-P2 pattern increases as the spatial heterogeneity of the initial condition increases (Fig 2C). Moreover, the Dis-P2 patterns are spatially random and selected by initial conditions. To quantify this property, we measured the spatial domain sizes (see Fig 2B for definition) from 2000 random trials for a given standard deviation of the spatial heterogeneity of the initial condition, and plotted the corresponding histogram in Fig 2D. It shows that the domain size can be any value as long as it is greater than a minimum domain size  $l_{\min}$ , i.e., the domain sizes distribute between  $l_{\min}$  and  $L - l_{\min}$ . Because of this randomness in pattern selection, the corresponding histogram of the global P2 amplitude ( $\Delta \bar{c}_{peak}$  as defined in Fig 2A) also exhibits a continuous distribution (Fig 2E).

**Effects of DGF on pattern selection and stability.** To investigate the effects of DGF on the spatiotemporal pattern dynamics, we carried out simulations by scanning the pacing period  $T$  and DGF strength  $\alpha$  (Fig 3A). There are four distinct regions: uniform P1 pattern (yellow), Con-P2 pattern only (cyan), Dis-P2 pattern only (black), and both concordant and discordant P2 (Con/Dis-P2) patterns (red). The blue curve is the stability boundary between P1 and P2 for an uncoupled FHN unit. For  $\alpha < 0$ , only uniform P1 and Con-P2 patterns were observed, independent of initial conditions. The uniform P1 and Con-P2 patterns are separated by the stability boundary (blue line) of the uncoupled FHN unit, indicating that the dynamics in the 1D array is the same as in the uncoupled FHN unit. For  $\alpha > 0$ , a transition from uniform P1 to Dis-P2 occurs as  $T$  decreases (from yellow to black), which is caused by a

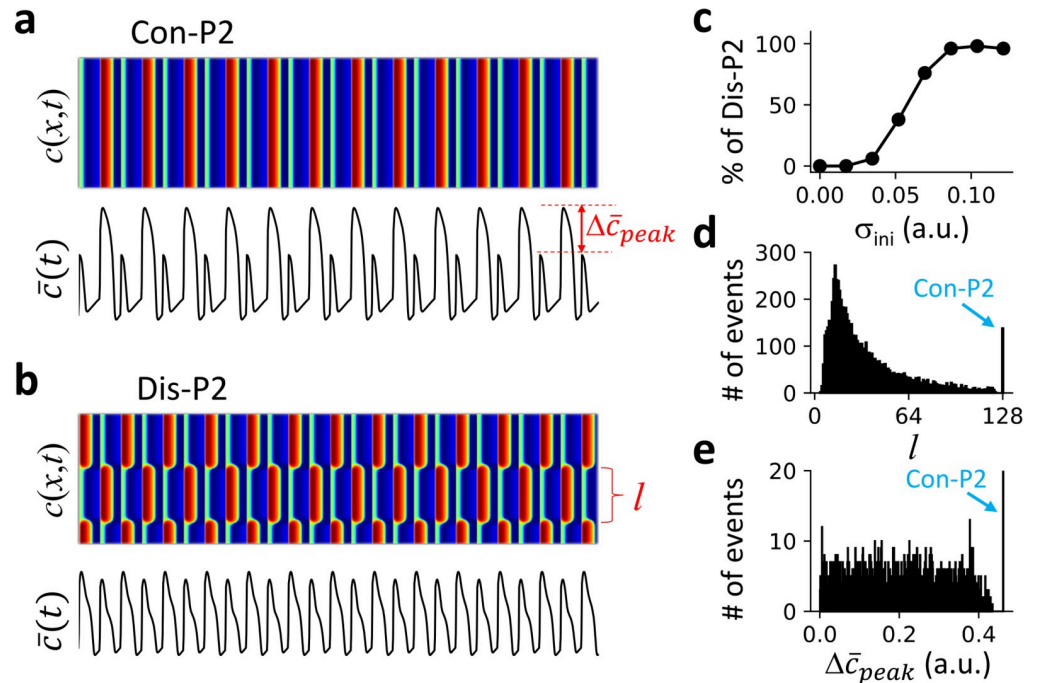


**Fig 2. Excitation patterns and dynamics in a 1D array of coupled FHN units without DGF.** The pacing period  $T = 45$  and system size  $L = 128$ . **a.** An example of Con-P2 patterns and the corresponding global signal  $\bar{c}(t)$ . **b.** An example of Dis-P2 patterns with a different initial condition from panel a, and the corresponding  $\bar{c}(t)$ . **c.** Percentage of Dis-P2 patterns versus the standard deviation ( $\sigma_{ini}$ ) of the random initial conditions.  $\sigma_{ini} = \delta/\sqrt{3}$ . We performed 100 trials for each  $\sigma_{ini}$  value in the plot. **d.** Histogram of domain size  $l$  (segment between two neighboring nodes, as indicated in panel b) from 2000 trials of random initial conditions with  $\delta = 0.15$ . For each trial, 2000 beats were applied for the system to reach a steady state. The domain size was measured using the last two beats. **e.** Histogram of global P2 amplitude  $\Delta\bar{c}_{peak}$  (difference between the peak values of two consecutive beats, as indicated in panel a) for the simulations in d.  $\Delta\bar{c}_{peak}$  was measured using the last two beats.

<https://doi.org/10.1371/journal.pcbi.1007931.g002>

spatial-mode instability of the uniform P1 state. As  $T$  decreases further (red region), both Con-P2 and Dis-P2 patterns can occur depending on the initial conditions (Fig 3B).

Furthermore, we performed the same statistical analysis as in the case of no DGF (Fig 2D and 2E) for different regions of the phase diagram in Fig 3A. In the Dis-P2 only region (Fig 3C), the domain sizes distribute between 0 to  $L/2$  (more accurately, the domain size can be  $L/2$  and any value between  $l_{min}$  and  $L/2 - l_{min}$ ), but  $\Delta\bar{c}_{peak}$  remains zero for all patterns. In the Con/Dis-P2 region (Fig 3D), the distributions are similar to those in Fig 3C except for the existence of the Con-P2 pattern. Similar to the case of no DGF ( $\alpha = 0$ ), the domain size distributions are continuous, indicating that the Dis-P2 patterns are spatially random (including the periodic ones) and depend on initial conditions. However, differing from the case of no DGF, the global signals of the Dis-P2 patterns are always P1 solutions i.e.,  $\Delta\bar{c}_{peak} = 0$  (Fig 3C and 3D). Moreover, the maximum domain size of Dis-P2 patterns is  $L/2$ . This is because if there is a domain greater than  $L/2$ , the sum of all other domains must be smaller than  $L/2$ , and thus when the patterns reverse in the next beat, the global signal cannot be the same, violating the requirement of a global P1 solution.

Therefore, in the absence of DGF ( $\alpha = 0$ ), both Con-P2 and Dis-P2 patterns can occur, and the Dis-P2 patterns are spatially random. In the presence of DGF, only Con-P2 patterns can exist when the DGF is negative ( $\alpha < 0$ ). When the DGF is positive ( $\alpha > 0$ ), both Con-P2 and Dis-P2 patterns can exist depending on the pacing period  $T$  and initial conditions. The Dis-P2 patterns are also spatially random but satisfy that the global signals are always P1 solutions.



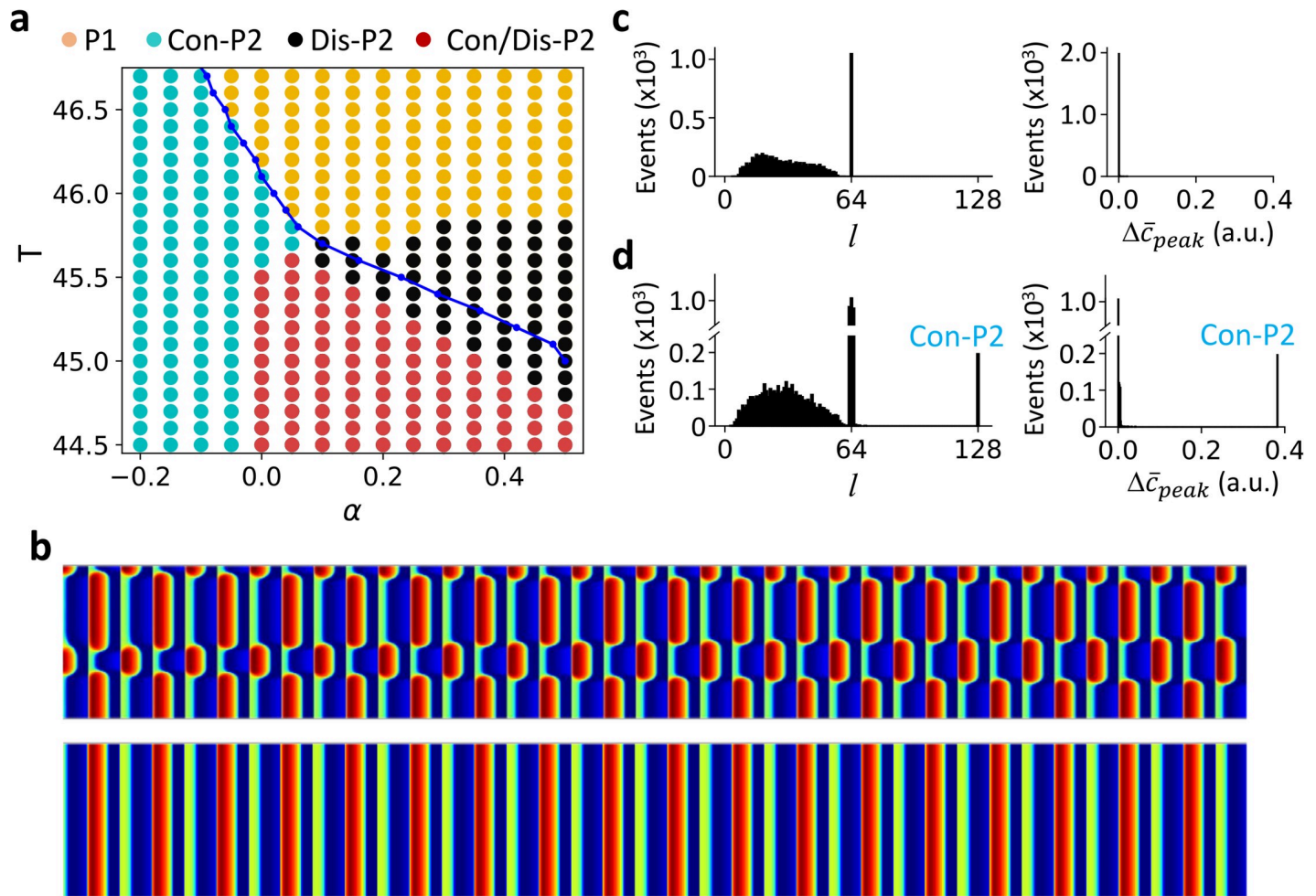


**Fig 3. Excitation patterns and dynamics in a 1D array of coupled FHN units with DGF.** **a.** Phase diagram of excitation dynamics. The blue line is the bifurcation boundary from P1 to P2 in an uncoupled unit with DGF. Color dots mark the different behaviors in the 1D array: yellow—uniform P1; black—Dis-P2; cyan—Con-P2; and red—Con/Dis-P2. **b.** A Dis-P2 pattern (upper) and a Con = P2 pattern (lower) for  $\alpha = 0.2$  and  $T = 45$  obtained with two different initial conditions. **c.** Left, histogram of domain size  $l$  from 2000 trials.  $\alpha = 0.4$  and  $T = 45.5$ . The random initial conditions were set the same way as described in Fig 2 legend with  $\delta = 3$ . For each trial, 2000 beats were applied for the system to reach a steady state. Right, corresponding histogram of global P2 amplitude  $\Delta \bar{c}_{peak}$  from the same simulations. **d.** Same as panel c but for  $\alpha = 0.2$ ,  $T = 45$ , and  $\delta = 0.09$ .

<https://doi.org/10.1371/journal.pcbi.1007931.g003>

### Ca<sup>2+</sup> release patterns in a physiologically detailed ventricular myocyte model

To validate the spatiotemporal dynamics in a realistic biological system, we carried out simulations in a physiologically detailed 3D ventricular myocyte model (see [Methods](#)), which can well capture the spatiotemporal Ca<sup>2+</sup> dynamics widely observed in experiments [29, 43–45]. The model undergoes a bifurcation from P1 to P2 (alternans) as the pacing period  $T$  decreases ([S2 Fig](#)). We investigated the subcellular Ca<sup>2+</sup> release patterns under both AP clamp and free-running conditions (see [S1 Text](#)). Under AP clamp, the voltage is no longer described by the differential equation but a pre-set function of time with a period  $T$  (see [S3 Fig](#) for the waveform used in this study). Under this condition, Ca<sup>2+</sup> is decoupled with voltage, and therefore, there is no DGF. Under the free-running condition, the cell is stimulated by a current pulse (0.5 ms duration and  $-80 \mu\text{A}/\mu\text{F}$  amplitude, see [Methods](#)), and voltage is a free running signal. Under this condition, Ca<sup>2+</sup> and voltage are coupled, and therefore, DGF is present due to Ca<sup>2+</sup> and

voltage coupling (as indicated in Fig 1B and 1C). The DGF properties can be changed by altering the ionic currents, as will be detailed below.

**Ca<sup>2+</sup> release patterns under AP clamp.** Under AP clamp, Ca<sup>2+</sup> is decoupled with voltage and thus no DGF. We used spatially random initial conditions to induce Dis-P2 patterns (see Fig 4 legend for the details of the random initial conditions). In the alternans regime (e.g., T = 300 ms), both Con-P2 (Fig 4A) and Dis-P2 (Fig 4B) patterns occur in the cell depending on initial conditions. The probability of forming a Dis-P2 pattern increases as the spatial heterogeneity of initial conditions increases (Fig 4C). The Dis-P2 patterns are spatially random as indicated by the histograms of domain size (Fig 4D) and whole-cell alternans amplitude  $\Delta\bar{c}_{peak}$

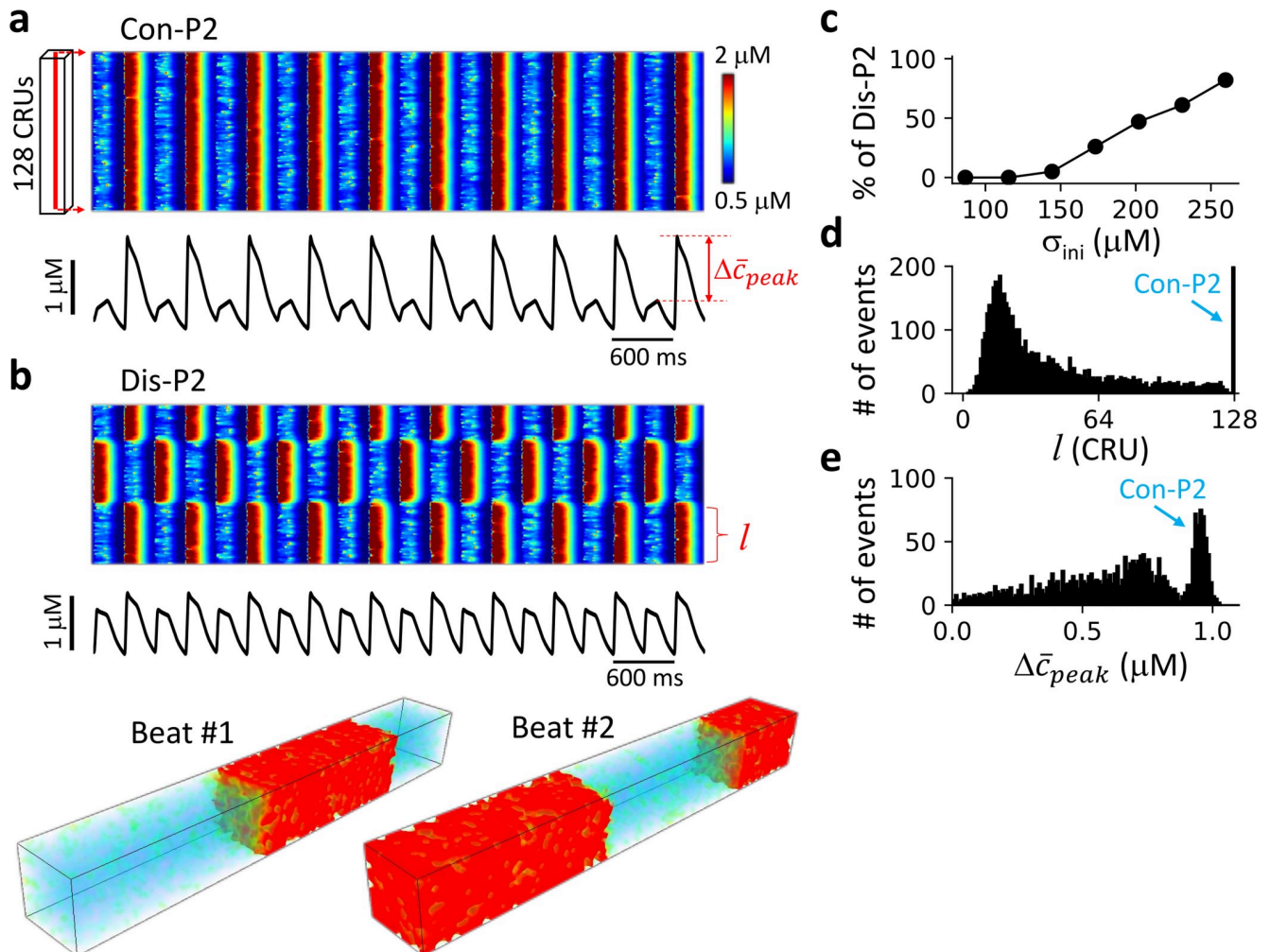


**Fig 4. Ca<sup>2+</sup> release patterns and dynamics in the 3D ventricular myocyte model under AP clamp.** **a.** Upper panel shows a linescan (time-space plot) of cytosolic Ca<sup>2+</sup> concentration showing a Con-P2 pattern. Lower panel shows the corresponding whole-cell Ca<sup>2+</sup> transient. The recording line was in the center of the cell as indicated on the left. **b.** Same as panel a. with a different random initial condition resulting in a Dis-P2 pattern. The middle panel is the corresponding whole-cell Ca<sup>2+</sup> transient. The bottom panels are 3D views of Ca<sup>2+</sup> from two consecutive beats. **c.** Percentage of Dis-P2 patterns versus the standard deviation ( $\sigma_{ini}$ ) of initial SR Ca<sup>2+</sup> load. The random spatial distribution of the SR Ca<sup>2+</sup> load was set as  $Ca_{SR}(j) = Ca_0 + \Delta Ca_{SR} \cdot \xi(j)$  ( $j = 1, 2, \dots, L$ ) with  $\xi(j)$  being a uniform random number in  $[-1, 1]$ .  $\sigma_{ini} = \Delta Ca_{SR} / \sqrt{3}$ . We set  $Ca_0 = 500 \mu\text{M}$ . We performed 100 trials for each  $\sigma_{ini}$  value in the plot. **d.** Histogram of domain size  $l$  (as marked in panel b) with  $\Delta Ca_{SR} = 450 \mu\text{M}$ . **e.** Histogram of global P2 amplitude  $\Delta\bar{c}_{peak}$  (as marked in panel a) from the same simulations in panel d. For panel d and e, 2000 trials were performed. For each trial, the cell was paced 2000 beats to reach a steady state. The domain size was computed using the last 50 beats to account for beat-to-beat variation (see SI for details) due to the intrinsic noise of ion channel stochasticity.  $\Delta\bar{c}_{peak}$  was measured using the last two beats. The pacing period T = 300 ms.

<https://doi.org/10.1371/journal.pcbi.1007931.g004>



(Fig 4E). These behaviors are the same as those for the model of coupled FHN units without DGF (Fig 2), albeit some smearing in the histograms due to ion channel stochasticity (see Methods).

#### **Ca<sup>2+</sup> release pattern dynamics with positive and negative Ca<sup>2+</sup>-to-APD coupling.**

Under free running, however, Ca<sup>2+</sup> is coupled with voltage, and changing Ca<sup>2+</sup> may change APD. If increasing the Ca<sup>2+</sup> transient amplitude results in a longer APD in the same beat, then it is called positive Ca<sup>2+</sup>-to-APD coupling, and the opposite is called negative Ca<sup>2+</sup>-to-APD coupling [46, 47]. As shown in previous studies [46, 48, 49], the coupling properties can be altered by altering the properties of I<sub>Ca</sub> and the Na<sup>+</sup>-Ca<sup>2+</sup> exchange current (I<sub>NCX</sub>). However, since I<sub>Ca</sub> and I<sub>NCX</sub> also directly affect the Ca<sup>2+</sup> dynamics, it becomes difficult to only change the Ca<sup>2+</sup>-to-APD coupling without affecting the Ca<sup>2+</sup> dynamics. To avoid this complexity, we added two new currents to the ventricular model: the non-specific Ca<sup>2+</sup>-activated cation current (I<sub>nsCa</sub>) and the small conductance Ca<sup>2+</sup>-activated potassium current (I<sub>SK</sub>). I<sub>nsCa</sub> is mainly an inward current [50] and increases as the intracellular Ca<sup>2+</sup> concentration increases. Therefore, increasing the conductance of I<sub>nsCa</sub> increases APD and promotes positive Ca<sup>2+</sup>-to-APD coupling. I<sub>nsCa</sub> is small under normal conditions but becomes large under conditions of Ca<sup>2+</sup> overload [50]. I<sub>SK</sub> is an outward current which also increases with the intracellular Ca<sup>2+</sup> concentration, and thus I<sub>SK</sub> promotes negative Ca<sup>2+</sup>-to-APD coupling. Under normal conditions, I<sub>SK</sub> only presents in atrial myocytes, but under heart failure, it also presents in ventricular myocytes [51–53]. Since the charge carriers of both currents are not Ca<sup>2+</sup>, unlike I<sub>Ca</sub> and I<sub>NCX</sub>, they do not directly affect intracellular Ca<sup>2+</sup> dynamics. Here we altered the maximum conductance of these two currents to alter the Ca<sup>2+</sup>-to-APD coupling properties. Note that DGF is not explicitly present in the model but indirectly via the Ca<sup>2+</sup>-to-APD coupling, as we explained in Introduction. We first investigated the effects of Ca<sup>2+</sup>-to-APD coupling properties on Ca<sup>2+</sup> release patterns and then linked them to DGF.

We systematically explored the spatiotemporal dynamics by altering the pacing period T and the maximum conductance of the two currents, as summarized in Fig 5A. We used the same spatially random initial conditions as in Fig 4 for the simulations. Note that due to dynamical instabilities and intrinsic noise of the sarcolemmal Ca<sup>2+</sup> channels and Ca<sup>2+</sup> release channels (see Methods), heterogeneous initial conditions are not needed for the formation of the Dis-P2 patterns in the Dis-P2 only region. When the Ca<sup>2+</sup>-to-APD coupling is negative (large I<sub>SK</sub>), a transition from uniform P1 to Con-P2 patterns occurs as T decreases, and this transition occurs at a larger T value as the maximum I<sub>SK</sub> conductance increases. When the coupling is positive (large I<sub>nsCa</sub>), a transition from uniform P1 to Dis-P2 patterns (yellow to black) occurs as T decreases. Under both coupling conditions, as T decreases further, the system enters the Con/Dis-P2 regime (red), in which both Con-P2 and Dis-P2 patterns can occur depending on initial conditions (Fig 5B). However, as T decreases even further, the Con/Dis-P2 regime switches into a Dis-P2 only regime when the Ca<sup>2+</sup>-to-APD coupling is negative (large I<sub>SK</sub>) and into a Con-P2 only region when the Ca<sup>2+</sup>-to-APD coupling is positive (large I<sub>nsCa</sub>). Therefore, for the same Ca<sup>2+</sup>-to-APD coupling, as T decreases, the spatiotemporal patterns change from Con-P2 only to Dis-P2 only through a Con/Dis-P2 region or in reverse order depending on the coupling properties.

To reveal the statistical properties of the Dis-P2 patterns, we show the histograms of domain sizes and the whole-cell alternans amplitude for a parameter point in the Dis-P2 region (Fig 5C) and a point in the Con/Dis-P2 region (Fig 5D). The domain size distributions for Dis-P2 patterns are continuous, and the whole-cell alternans amplitudes always remain zero, indicating that the patterns are spatially random but always satisfy that the global signals are P1 solutions. These behaviors are the same as in the model of a coupled array of FHN units (Fig 3).

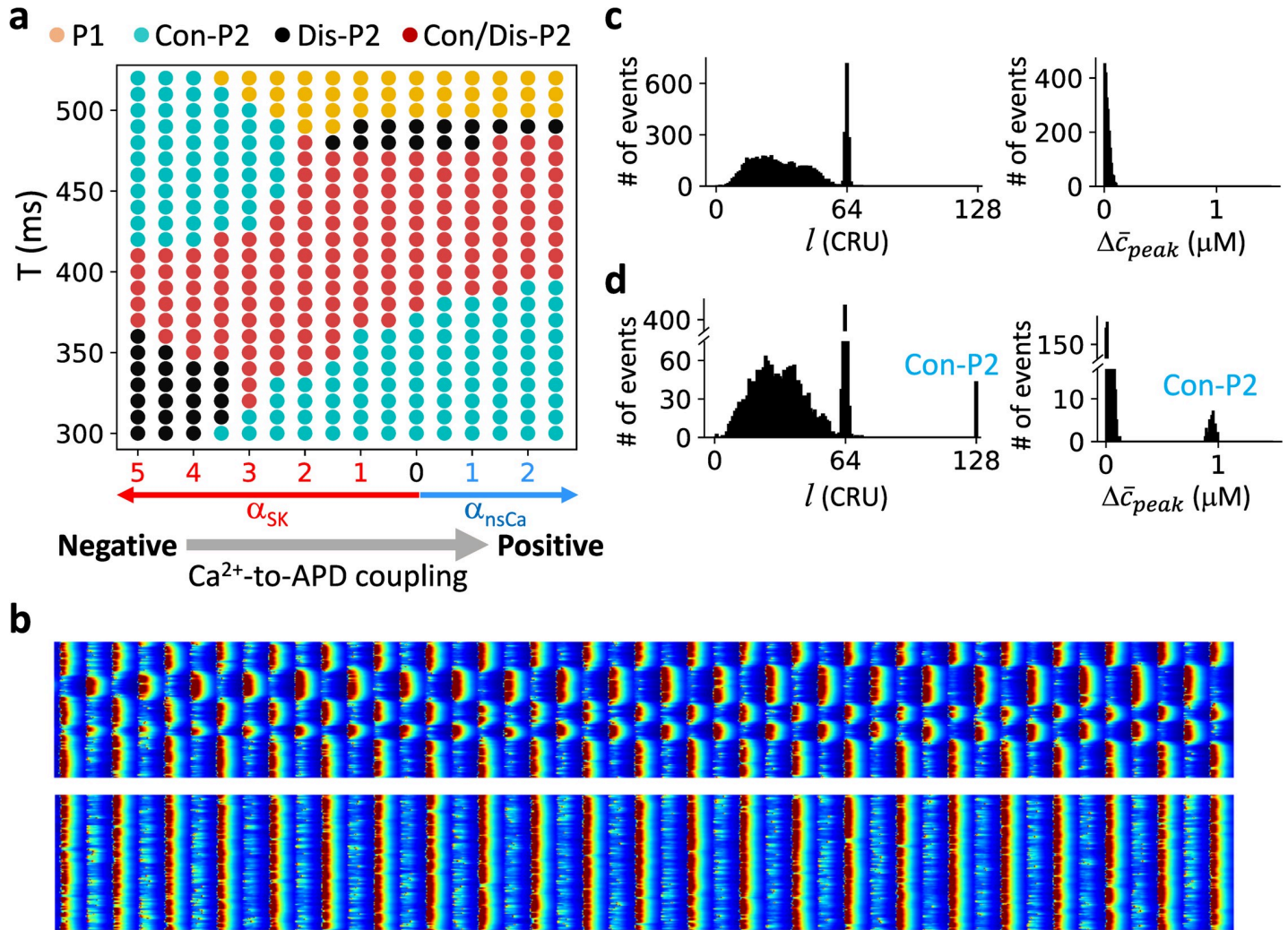


**Fig 5. Ca<sup>2+</sup> release pattern dynamics in the ventricular myocyte model with positive and negative Ca<sup>2+</sup>-to-APD coupling.** a. Phase diagram of Ca<sup>2+</sup> release dynamics versus pacing period and Ca<sup>2+</sup>-to-APD coupling properties. In this diagram, the x-axis is the fold increase of either I<sub>nsCa</sub> (blue arrow) or I<sub>SK</sub> (red arrow), and the y-axis is the pacing period T. Gray arrow indicates the change from negative to positive Ca<sup>2+</sup>-to-APD coupling. Same color codes of the pattern dynamics as in Fig 3A were used. b. A Dis-P2 pattern (upper) and a Con = P2 pattern (lower) for α<sub>SK</sub> = 3.5 and T = 350 ms obtained with two different initial conditions. c. Left: Histogram of domain size l. The pacing period T = 330 ms, α<sub>SK</sub> = 4.5. The random initial conditions were set the same way as in Fig 4 with ΔC<sub>aSR</sub> = 500 μM. Two thousand trials were performed. For each trial, the cell was paced 2000 beats to reach a steady state. The domain size was computed using the last 50 beats. Right: Histogram of global P2 amplitude Δc̄<sub>peak</sub> from the same simulations. Δc̄<sub>peak</sub> was measured using the last two beats. d. Same as panel c but T = 350 ms and α<sub>SK</sub> = 3.5.

<https://doi.org/10.1371/journal.pcbi.1007931.g005>

**Linking the Ca<sup>2+</sup>-to-APD coupling properties to DGF.** As shown above, the Ca<sup>2+</sup> dynamics in the detailed ventricular myocyte model agree well with those of the generic FHN array with DGF. To link the spatiotemporal Ca<sup>2+</sup> dynamics to the DGF properties, we performed a quantitative analysis to reveal the DGF properties and their relationship with the Ca<sup>2+</sup>-to-APD coupling properties. We carried out simulations of the ventricular cell model using an S1S2 protocol. In this protocol, a train of external stimuli (S1) was given at a fixed period (T = 300 ms) for the cell to reach the steady state, and a stimulus (S2) was then applied after a variable interval (denoted as S1S2 interval) from the last S1 beat. We measured the peak values of I<sub>Ca</sub>, SR Ca<sup>2+</sup> and cytosolic Ca<sup>2+</sup> on the S2 beat, which were considered as control. Next, we repeated the same simulations except that on the last S1 beat, we increased α<sub>SK</sub> to shorten the APD (Fig 6A, red) or increased α<sub>nsCa</sub> to lengthen the APD (Fig 6A, cyan). This

method enhanced the negative (increased  $\alpha_{SK}$ ) or the positive (increased  $\alpha_{nsCa}$ )  $Ca^{2+}$ -to-APD coupling from the control case. In Fig 6C, we plot the ratios of the peak values of  $I_{Ca}$ , SR  $Ca^{2+}$  and cytosolic  $Ca^{2+}$  of the two coupling cases to the control values on the S2 beat.

For short S1S2 intervals (e.g., S1S2 = 200 ms, Fig 6A), the enhanced positive  $Ca^{2+}$ -to-APD coupling case (cyan) results in a smaller  $I_{Ca}$  (ratio < 1, see Fig 6C, top panel) and almost unchanged SR load compared to those of the control case on the S2 beat. The reason is that the longer APD caused by the positive  $Ca^{2+}$ -to-APD coupling results in a shorter DI and thus less recovery of  $I_{Ca}$ . The net effect is to result in a smaller  $Ca^{2+}$  transient (ratio < 1, see Fig 6C, bottom panel) than that of the control case because of a smaller  $I_{Ca}$ . This indicates that the global feedback results in a negative gain on the  $Ca^{2+}$  signal on the next beat, i.e., the DGF is negative. For the negative  $Ca^{2+}$ -to-APD coupling case (Fig 6A, red), the consequences are reversed, resulting in a positive DGF (Fig 6C, bottom panel). These results suggest that for short S1S2 intervals, the DGF properties are primarily determined by the recovery property of  $I_{Ca}$ .

For long S1S2 intervals (e.g., S1S2 = 500 ms, Fig 6B), the  $Ca^{2+}$ -to-APD coupling properties have negligible effects on  $I_{Ca}$  (both ratios are  $\sim 1$ , see Fig 6C, top panel) since  $I_{Ca}$  fully recovers due to a long DI. However, the SR  $Ca^{2+}$  load is lower (ratio < 1) for the negative  $Ca^{2+}$ -to-APD coupling and higher (ratio > 1) for the positive  $Ca^{2+}$ -to-APD coupling (Fig 6C, middle panel). Therefore, for the negative  $Ca^{2+}$ -to-APD coupling case, the feedback results in a smaller  $Ca^{2+}$  in the next beat because of a lower SR  $Ca^{2+}$  load, i.e., the DGF is negative. For the positive  $Ca^{2+}$ -to-APD coupling case, the DGF is positive. These results suggest that for long S1S2 intervals, the DGF properties are primarily determined by the SR  $Ca^{2+}$  load.

Therefore, for short S1S2 intervals (<300 ms), positive or negative  $Ca^{2+}$ -to-APD coupling leads to negative or positive DGF, respectively, primarily mediated by  $I_{Ca}$  recovery. For long S1S2 intervals (>300 ms), the relationships are reversed, i.e., positive or negative  $Ca^{2+}$ -to-APD coupling leads to positive or negative DGF, respectively. The DGF is primarily mediated by SR  $Ca^{2+}$  load since with long S1S2 intervals the  $Ca^{2+}$ -to-APD coupling properties show almost no effects on  $I_{Ca}$  due to full recovery. Knowing the relationships between  $Ca^{2+}$ -to-APD coupling properties and the DGF properties, one can then link the DGF properties to the  $Ca^{2+}$  release patterns in the ventricular cell model. Based on the analysis above and the  $Ca^{2+}$  release patterns shown in Fig 5A, we can link the  $Ca^{2+}$  release patterns to the sign of DGF, which is summarized in Table 1. It shows that negative DGF leads to Con-P2 patterns, while positive DGF leads to Dis-P2 patterns. Note that we were not able to quantitatively distinguish the boundaries between positive and negative DGF in the phase diagram (Fig 5A) using this analysis, but it is likely that in the Con/Dis-P2 region, the DGF is also positive. Therefore, we can obtain the same conclusion as that from the generic FHN model.

## Theoretical insights from a CML model

To reveal analytically the instabilities and bifurcations leading to the spatiotemporal dynamics, we used a CML model to describe the system. CML, as a generic model for investigating spatiotemporal dynamics of nonlinear systems, has been widely used [54, 55]. In a previous study [56], we developed a CML model to investigate the spatiotemporal APD dynamics in cardiac tissue. Here we modified the 1D array CML model by adding a DGF term. The governing equation is,

$$c_n(j) = f[c_{n-1}(j)] + \sum_{m=-M}^M w_m [f[c_{n-1}(j+m)] - f[c_{n-1}(j)]] - \alpha [f(\bar{c}_{n-1}) - f(\bar{c}_s)] \quad (4)$$

where  $n$  is the temporal index and  $j$  the spatial index.  $c_n(j)$  describes the peak signal in the  $j^{\text{th}}$  lattice of the  $n^{\text{th}}$  beat.  $f$  is the map function:  $f(c_n) = 0.2 + \frac{0.8}{1 + e^{(\bar{c}_n - \gamma)/\mu}}$  in which  $\gamma$  and  $\mu$  determine the midpoint and the slope of the curve, respectively.  $M$  is the coupling length, and  $w_m$  is the

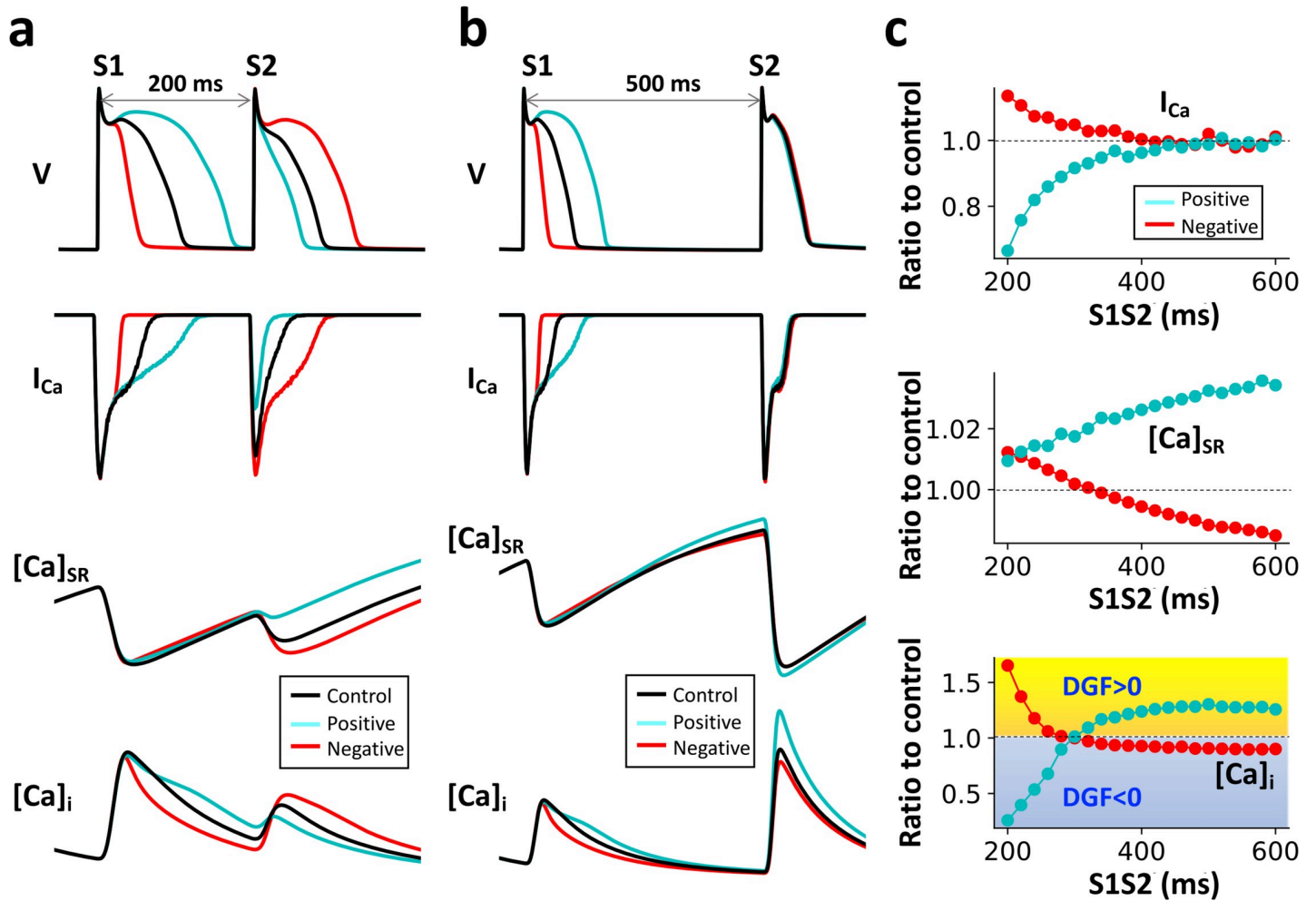


**Fig 6. Relationship between the Ca<sup>2+</sup>-to-APD coupling properties and DGF.** **a.** Time traces of voltage, I<sub>Ca</sub>, SR Ca<sup>2+</sup>, and cytosolic Ca<sup>2+</sup> for control (black), enhanced positive coupling in the S1 beat (cyan) and enhanced negative coupling in the S1 beat (red). S1S2 = 200 ms. **b.** Same as in a. but S1S2 = 500 ms. **c.** Ratios of I<sub>Ca</sub> peak, SR Ca<sup>2+</sup> load, and [Ca<sup>2+</sup>]<sub>i</sub> peak on the S2 beat under positive (cyan) or negative (red) coupling conditions to the corresponding quantities at control v.s. S1S2 interval. Here, α<sub>nsCa</sub> = 0 for all the cases. In the S1 beat, α<sub>SK</sub> is 5, 0, and 30 for control, enhanced positive, and enhanced negative cases, respectively. In the S2 beat, α<sub>SK</sub> is 5 for all the cases.

<https://doi.org/10.1371/journal.pcbi.1007931.g006>

coupling strength described by a Gaussian function:  $w_m = \frac{e^{-m^2/2\sigma^2}}{\sqrt{2\pi\sigma N_w}}$  in which  $N_w$  is the normalization constant.  $\bar{c}_{n-1}$  is the spatial average of  $c_{n-1}(j)$ , and  $\bar{c}_s = c_s$  satisfying  $c_s = f(c_s)$ . We set  $\mu = 0.1$ ,  $M = 15$ , and  $\sigma = 3$ . Note that concrete forms of map functions for investigating intracellular Ca<sup>2+</sup> dynamics were developed previously [47, 57]. However, for the sake of simplicity and generality, we chose a simple function  $f$ , which can give rise to a bifurcation from P1 to P2, similar to those of the FHN model and the detailed ventricular myocyte model (see S2 Fig).

**Table 1. Links between Ca<sup>2+</sup>-to-APD coupling, Ca<sup>2+</sup> release patterns, and DGF for the detailed ventricular cell model.** The sign in parenthesis is the sign of DGF.

	Negative Ca <sup>2+</sup> -to-APD coupling	Positive Ca <sup>2+</sup> -to-APD coupling
Slow pacing	Con-P2, DGF (-)	Dis-P2, DGF (+)
Fast pacing	Dis-P2, DGF (+)	Con-P2, DGF (-)

<https://doi.org/10.1371/journal.pcbi.1007931.t001>



Note that in Eq 4, instead of using a linear feedback term:  $\alpha(\bar{c}_{n-1} - \bar{c}_s)$ , we used a nonlinear term with the map function  $f$ , i.e.,  $-\alpha[f(\bar{c}_{n-1}) - f(\bar{c}_s)]$ , to maintain the convergence of iteration. The negative sign was used because  $f$  is a decreasing function ( $f' < 0$ ). Linearization of this nonlinear term around the uniform steady-state gives rise to a term proportional to  $\alpha(\bar{c}_{n-1} - \bar{c}_s)$ , and thus  $\alpha > 0$  corresponds to positive feedback, the same as in the FHN model.

1) *Stability of an uncoupled unit.* For an uncoupled unit, the map equation with DGF becomes

$$c_n = f(c_{n-1}) - \alpha[f(c_{n-1}) - f(c_s)] \tag{5}$$

The stability of the steady-state solution is determined by the eigenvalue,

$$\lambda = (1 - \alpha)f' \tag{6}$$

where  $f' = \frac{df}{dc_n} |_{c_n=c_s}$ .  $f'$  is independent of  $\alpha$  since the steady state is independent of  $\alpha$ . Eq 6 indicates that  $\alpha < 0$  destabilizes the steady state, and  $\alpha > 0$  stabilizes the steady state. The stability boundary is shown as the dashed line in Fig 7A.

2) *Stability of the spatially uniform P1 state.* The spatially uniform P1 state (see Stability analyses of the CML model in SI) is determined by the eigenvalues:

$$\lambda_k = \begin{cases} (1 - \alpha)f', & \text{for } k = 0 \\ \left(1 - 4 \sum_{m=1}^M w_m \sin^2 \frac{\pi mk}{L}\right) f', & \text{for } k = 1, 2, \dots, L - 1 \end{cases} \tag{7}$$

in which  $k$  is the wave number of the Fourier mode ( $\lambda_k$  vs.  $k$  for different  $\alpha$  values are shown in S4 Fig). The spatially uniform P1 state is stable when  $|\lambda_k| < 1$  for any  $k$ . The stability of the 0-mode is the same as that of an uncoupled unit. Since  $\lambda_k$  for  $k > 0$  in Eq 7 does not depend on  $\alpha$ , then the feedback has no effects on the stability of the uniform P1 state for non-zero mode. Because of this, the stability boundary separating uniform P1 from Dis-P2 appears to be a horizontal line independent of  $\alpha$  (Fig 7A, solid).

3) *Stability of the Con-P2 state.* Following the same procedure as for the uniform P1 state, we obtained the eigenvalues for the spatially uniform P2 state as

$$\lambda_k = \begin{cases} (1 - \alpha)^2 f'_1 f'_2, & \text{for } k = 0 \\ \left(1 - 4 \sum_{m=1}^M w_m \sin^2 \frac{\pi mk}{L}\right)^2 f'_1 f'_2, & \text{for } k = 1, 2, \dots, L - 1 \end{cases} \tag{8}$$

where  $f'_1$  and  $f'_2$  are the two derivatives of  $f$  at the P2 solution of Eq 5. Since the P2 solution depends on  $\alpha$ ,  $f'_1$  and  $f'_2$  are functions of  $\alpha$ . Therefore, the stability boundary also depends on  $\alpha$  (Fig 7A, dashed-dotted).

4) *Stability of the Dis-P2 states.* The stability of the Dis-P2 states cannot be analytically obtained. We used numerical simulations of the CML model (Eq 4) to determine the stability boundary (Fig 7A, dotted). No stable Dis-P2 patterns were obtained on the left side of the dotted line.

Spatiotemporal dynamics via numerical simulations of the CML model are also shown in Fig 7A, which are colored the same way as in Fig 3A and Fig 5A. The Dis-P2 only region exists between the uniform P1 stability boundary (solid line) and the Con-P2 stability boundary (dash-dotted line). The Con/Dis-P2 region exists between the Con-P2 stability boundary (dashed-dotted line) and the Dis-P2 stability boundary (dotted line). The Con-P2 only region exists between the uniform P1 stability boundary (dashed line) and the Dis-P2 stability boundary (dotted line). Note that the dotted line is almost identical to  $\alpha = 0$  except at the vicinity



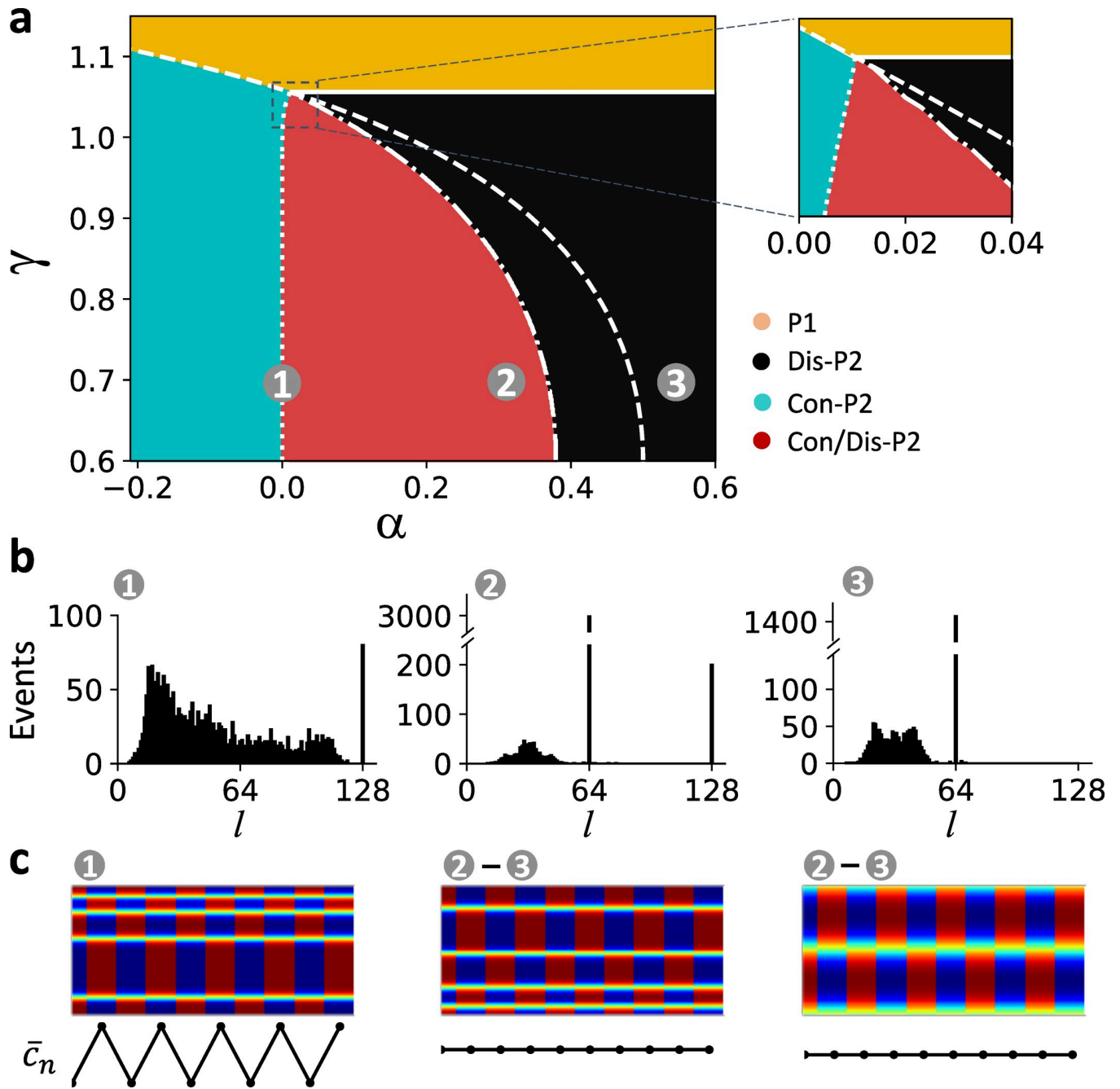


**Fig 7. Bifurcations and spatiotemporal dynamics in the CML model.** **a.** Phase diagram in the  $\alpha$ - $\gamma$  space showing stability boundaries and spatiotemporal dynamics of the CML model. The same color codes as in Fig 3A and Fig 5A were used. The solid line is the stability boundary of uniform P1 determined by Eq 7. The dashed line is the stability boundary of P1 in an uncoupled unit determined by Eq 6. The dash-dot line is the stability boundary of Con-P2 determined by Eq 8. The vertical dotted line is the stability boundary of Dis-P2 determined by numerical simulations of the CML model. Inset is the blowup of the marked region, showing that all the stability boundaries meet at a common point. **b.** Histograms of domain size at different locations in the phase diagram marked by numbers. The coordinates  $(\alpha, \gamma)$  from location 1 to 3 are: (0, 0.7), (0.3, 0.7), and (0.55, 0.7). **c.** Sample spatiotemporal patterns (top) and the corresponding global signals (bottom) from different regions of the phase diagram. Number ranges above each pattern indicate the locations in the phase diagram where the specific pattern can be seen.

<https://doi.org/10.1371/journal.pcbi.1007931.g007>

where all phases meet (inset in Fig 7A), indicating that stable Dis-P2 patterns can only exist when  $\alpha > 0$ . Histograms of domain size and example spatial patterns from three locations

marked in Fig 7A are plotted (Fig 7B and 7C). The structure of the phase diagram and the statistical properties of the spatial patterns of the CML model match well with those of the generic FHN model and the ventricular myocyte model.

## Discussion

We investigated the roles of DGF in the genesis, selection, and stability of spatiotemporal patterns in periodically-paced excitable media. We used three models with different complexities, which allowed us to perform both numerical simulations and rigorous analytical treatments. The dynamical behaviors are well conserved in the three types of models, and the CML model reveals the dynamical mechanisms. Our major findings are as follows:

1. In the absence of DGF, both Con-P2 and Dis-P2 can occur depending on the pacing period and initial conditions. The Dis-P2 patterns are spatially random, determined by the initial conditions. The global signal (the spatial average) is a temporal P2 solution (alternans) with the alternans amplitude being randomly distributed between zero and the maximum amplitude (Con-P2).
2. In the presence of DGF, the pattern dynamics are determined by the sign of the DGF. When the DGF is negative, only Con-P2 patterns can exist, no spatial mode instabilities emerge, and all the Dis-P2 solutions are unstable. When the DGF is positive, both Con-P2 and Dis-P2 patterns can occur, depending on the pacing period and initial conditions. The Dis-P2 patterns are also spatially random but must satisfy that the global signals are temporal P1 solutions (no temporal alternans).
3. Bifurcation analyses of the CML model reveal the spatial-mode instabilities leading to the spatiotemporal patterns.
4. By linking the  $\text{Ca}^{2+}$ -to-APD coupling properties to the DGF properties, we have shown that the spatiotemporal pattern dynamics of  $\text{Ca}^{2+}$  release in cardiac myocytes agree very well with the findings in the simple models, validating the theoretical predictions in a realistic system.

Therefore, our simulations and theoretical analyses reveal the underlying dynamical mechanisms and roles of DGF in the genesis, selection, and stability of spatiotemporal patterns in periodically-paced excitable media. The uniqueness of the conclusions drawn from the three types of models implies that the insights obtained in this study may apply to many excitable as well as oscillatory biological media. Here we discuss two examples below.

### A unified theory for subcellular $\text{Ca}^{2+}$ alternans dynamics in cardiac myocytes

At the subcellular level, both Con-P2 and Dis-P2  $\text{Ca}^{2+}$  release patterns (spatially concordant and discordant alternans) have been observed experimentally [31–33, 58, 59], but the underlying mechanisms remain incompletely understood. As shown in this study, the subcellular  $\text{Ca}^{2+}$  alternans dynamic of the ventricular myocyte model agree well with those of the simplified models, indicating that the generic mechanisms of pattern formation and selection are also applicable to  $\text{Ca}^{2+}$  alternans dynamics in cardiac myocytes. Both spatially concordant and discordant  $\text{Ca}^{2+}$  alternans (Con-P2 and Dis-P2 patterns) have been observed experimentally in cardiac myocyte [31–33, 59]. Shiferaw and Karma [60] developed a theory showing that a Turing instability caused by negative  $\text{Ca}^{2+}$ -to-APD coupling is responsible for the formation of Dis-P2 patterns. A direct experimental demonstration of this theory was carried out by Gaeta et al. [33], who developed a method that could change the sign of  $\text{Ca}^{2+}$ -to-APD coupling. However, Dis-P2 patterns have also been observed experimentally under voltage-clamp

[32, 59] and free-running conditions without showing negative coupling [61]. Furthermore, previous simulation studies [44, 48] and this study have also shown that Con-P2 patterns can occur under negative  $\text{Ca}^{2+}$ -to-APD coupling, and Dis-P2 patterns can occur under positive  $\text{Ca}^{2+}$ -to-APD coupling and voltage-clamp conditions. These complex  $\text{Ca}^{2+}$  release behaviors cannot be well explained by the Turing instability mechanism alone. On the other hand, our study unifies the complex subcellular  $\text{Ca}^{2+}$  alternans dynamics under a single theoretical framework of DGF, providing a general mechanistic understanding of the subcellular  $\text{Ca}^{2+}$  alternans dynamics.

Previous studies [33, 48, 60] showed that the sign of  $\text{Ca}^{2+}$ -to-APD coupling determines the occurrence of subcellular discordant  $\text{Ca}^{2+}$  alternans. One can achieve this by properly tuning the relative contributions of  $I_{\text{Ca}}$  and  $I_{\text{NCX}}$  [48, 49, 60]. Here we show that changing the maximum conductance  $I_{\text{SK}}$  or  $I_{\text{nsCa}}$  provides a more straightforward way of changing the coupling properties. Gaeta et al. [33] used a feedback control method to alter the coupling relationship and demonstrated in both simulations and experiments that the sign of the coupling controls the transitions between concordant and discordant  $\text{Ca}^{2+}$  alternans. However, our study shows that altering the  $\text{Ca}^{2+}$ -to-APD coupling properties does not guarantee that one can control the transition between concordant and discordant  $\text{Ca}^{2+}$  alternans. The unique dynamical factor controlling the transition between concordant and discordant  $\text{Ca}^{2+}$  alternans is the sign of DGF, which is not uniquely determined by the sign of  $\text{Ca}^{2+}$ -to-APD coupling. This is because  $\text{Ca}^{2+}$ -to-APD coupling affects the recovery of  $I_{\text{Ca}}$  and SR  $\text{Ca}^{2+}$  loading which contribute oppositely to DGF.

### Applications to tissue-scale dynamics of excitable biological media

Cardiac and neural tissue are typical excitable media. In cardiac tissue, spatially concordant and discordant APD alternans have been widely observed in experiments [37, 62–64], and mechanisms have been revealed in mathematical modeling and theoretical studies [38, 65, 66]. However, in the real heart, electrical excitations cause mechanical contraction, and the contraction and stretch of the heart cells may result in the opening of the mechano-sensitive ion channels or alteration of intracellular  $\text{Ca}^{2+}$  cycling properties, a phenomenon called mechano-electric feedback [34–36]. Since contraction is a mechanical response of cardiac tissue, which is nearly a global signal, it is possible that the mechano-electric feedback can serve as global feedback or a DGF to affect the discordant APD alternans dynamics. This needs to be investigated in future studies using models with mechano-electric feedback [67–69].

In neural tissue, cluster firing and other firing patterns have been widely observed [70–73]. The role of delayed feedback or DGF in the formation of firing patterns has been investigated in computer models [39–41]. In a simulation study by Golomb and Rinzel [42], the authors showed similar Dis-P2 patterns of firing as the discordant patterns shown in our present study. We believe that the theoretical insights from our simple FHN model or the CML model will help shed light on the formation of the firing patterns.

### Links to pattern dynamics in oscillatory media with DGF

Our study focused on the roles of DGF in pattern formation and stability in periodically-paced excitable media. In a previous study in oscillatory chemical reaction experiments, Kim et al. [17] showed DGF caused clustering patterns similar to the Dis-P2 patterns in this study. Their observations were also demonstrated in computer simulations [19]. Since, in their studies, the DGF is an externally controlled signal, the delay time is a variable parameter. However, the DGF is intrinsic in the excitable biological media we investigated, and the delay time is simply the excitation period. Because of this, we can represent the system with a CML model that is

able to capture the dynamics and the underlying bifurcations accurately. Since an excitable medium can become an oscillatory medium, the theories from our study may provide mechanistic insights into pattern dynamics of oscillatory media, such as the cluster patterning in the chemical reactions [14–19] or neural tissue [42].

### Methods

The present study involved three mathematical models at different levels of complexity. The model of a coupled array of FHN units and the 1D CML model are described in the Result section. A brief summary of the 3D ventricular cell model and numerical methods is given below.

#### The 3D ventricular cell model

The ventricular cell model has been described in detail in our previous studies [44, 45], similar to other previous models [74–78]. Here we give a brief description of the model. The 3D cell model consists of 128×16×16 CRUs. Each CRU includes five sub-compartments: bulk cytosol, submembrane, dyad, junctional SR and network SR. The volumes of these sub-compartments are based on experimental data. The Ca<sup>2+</sup> within a CRU cycles through these sub-compartments via diffusion, buffering/unbuffering, SR release and SERCA pump. The flow of Ca<sup>2+</sup> between CRUs is via diffusion in the cytosol, submembrane and network SR. The exchange of Ca<sup>2+</sup> between intracellular and extracellular space is regulated by I<sub>Ca</sub> and Na<sup>+</sup>-Ca<sup>2+</sup> exchanger (NCX). The model is described by differential equations that are coupled via Ca<sup>2+</sup> and voltage. The closing and opening of L-type Ca<sup>2+</sup> channels and the ryanodine receptors are simulated using stochastic Markov transitions. Therefore, intrinsic spatiotemporal noise exists in the model.

We added two new currents, *I<sub>nsCa</sub>* and *I<sub>SK</sub>*, to the model for altering Ca<sup>2+</sup>-to-APD coupling. The *I<sub>nsCa</sub>* formulation was adopted from the 1994 Luo and Rudy model [50] with the following parameter changes: P<sub>ns(Ca)</sub> = 3.5×10<sup>-5</sup> cm/s and K<sub>m,ns(Ca)</sub> = 1.5 μM. *I<sub>SK</sub>* was formulated based on Komendantov et al. [79] as follows:

$$I_{SK} = G_{SK} \frac{1}{1 + \left(\frac{K_d}{[Ca^{2+}]_i}\right)^4} (V - E_K), \tag{9}$$

where *G<sub>SK</sub>* = 0.005 mS/F and *K<sub>d</sub>* = 0.6 μM.

The differential equation for voltage is then

$$C_m \frac{dV}{dt} = - \left( I_{Na} + I_{Ca,L} + I_{Ks} + I_{Kr} + I_{NCX} + I_{NaK} + I_{K1} + I_{to,f} + I_{to,s} + I_{Cab} + \alpha_{nsCa} I_{nsCa} + \alpha_{SK} I_{SK} + I_{sti} \right) \tag{10}$$

where *C<sub>m</sub>* = 1 μF/cm<sup>2</sup> is the membrane capacitance. α<sub>nsCa</sub> and α<sub>SK</sub> are the parameters controlling the maximum conductance of *I<sub>nsCa</sub>* and *I<sub>SK</sub>*, respectively. *I<sub>sti</sub>* is the stimulus current density which is a square pulse with the amplitude -80 μA/μF and the duration 0.5 ms.

#### Computer simulations and algorithms

Both the model of a coupled array of FHN units and the CML model were programmed with Python 3, and the corresponding simulations were carried out on our cluster with 24 Intel Xeon CPUs. The 3D ventricular cell model was programmed with CUDA C++, and the corresponding simulations were carried out on Nvidia Tesla K20c, K80, and GTX 1080 Ti GPU cards. The detailed algorithms for detecting spatiotemporal excitation patterns in this study are described in the S1 Text and S5 Fig.

## Supporting information

**S1 Text.** The online supporting information includes: **A.** AP clamp and free running protocols. **B.** Stability analysis of the CML model. **C.** Automatic detection algorithms for spatiotemporal excitation patterns. **D.** Boundary between discordant P2 and uniform P2 in the CML model.

(DOCX)

**S1 Fig. Examples of spatiotemporal  $\text{Ca}^{2+}$  release dynamics in excitable biological systems.**

**a).** Data from Roome et al.[1] showing a spatiotemporal map of spontaneous dendritic voltage signal obtained from 5 s of linescan recording. Filled triangles indicate dendritic complex spikes (DCS). Subthreshold dendritic voltage modulation is also visible in the spatiotemporal voltage map. Red trace shows spatially averaged voltage, recorded at 2 kHz resolution. Corresponding spatiotemporal map for dendritic  $\text{Ca}^{2+}$  is also recorded. Green trace shows spatially averaged  $\text{Ca}^{2+}$ . **b).** Data from Diaz et al.[2] showing spatiotemporal  $\text{Ca}^{2+}$  signals under control and ryanodine receptor blocker tetracaine with a voltage clamp protocol. Linescan recordings reveal out-of-phase spatial patterns of intracellular  $\text{Ca}^{2+}$  transient from beat to beat. Bottom two traces show fluorescence measured as a function of time at the regions indicated by arrows (i and ii).

(EPS)

**S2 Fig. Bifurcation diagrams for the FHN, detailed ventricular myocyte and CML models.**

**a).** Bifurcation diagram showing  $c$  vs.  $T$  for the single-element FHN model. **b).** Bifurcation diagram showing the peak values of the whole-cell average  $\text{Ca}^{2+}$  transient,  $\bar{c}_p$  vs.  $T$  for the detailed ventricular myocyte model. **c).** Bifurcation diagram showing  $c$  vs.  $\gamma$  for the single-element CML model.

(EPS)

**S3 Fig. Time trace of membrane voltage used in the AP clamp protocol for the detailed cell model.** The voltage trace is the last action potential recorded in the simulation of the physiologically detailed myocyte model. The model was paced for 100 beats to reach the steady state at the pacing period  $T = 450$  ms. This voltage trace was used in the AP clamp simulations.

(EPS)

**S4 Fig.  $\lambda_k$  vs. the wave number  $k$  for the 1D CML model under the P1 regime.**  $\lambda_k$  vs.  $k$  for  $\alpha = 0.2$  (black), 0 (red) and  $-0.2$  (blue) are numerically computed based on Eq 7 in the main text.  $\gamma = 1.057$ , which is the bifurcation point in S2C Fig.

(EPS)

**S5 Fig. Illustration of domain size detection by the pattern recognition algorithm.** **a).** Top shows an example of discordant P2 patterns for the 1D FHN model. Bottom shows the relationship of  $\Delta c_{n+1}(j)$  vs.  $j$  where the domain size  $l$  determined by the pattern recognition algorithm is marked by the double-arrow red line. **b).** Same as a), but for the 1D CML model. **c).** Same as a), but for the detailed myocyte model. Note that the gray and black traces are for  $m = 1$  and 50 in S10 Eq, respectively. We used  $m = 50$  to extract the domain size for the detailed myocyte model in our study.

(EPS)

## Author Contributions

**Conceptualization:** Zhen Song, Zhilin Qu.

**Data curation:** Zhen Song.



**Formal analysis:** Zhen Song, Zhilin Qu.

**Funding acquisition:** Zhilin Qu.

**Investigation:** Zhen Song, Zhilin Qu.

**Methodology:** Zhen Song, Zhilin Qu.

**Project administration:** Zhen Song, Zhilin Qu.

**Resources:** Zhilin Qu.

**Software:** Zhen Song.

**Supervision:** Zhilin Qu.

**Validation:** Zhen Song, Zhilin Qu.

**Visualization:** Zhen Song, Zhilin Qu.

**Writing – original draft:** Zhen Song, Zhilin Qu.

**Writing – review & editing:** Zhen Song, Zhilin Qu.

## References

1. Wolpert L. Pattern Formation in Biological Development. *Sci Am.* 1978; 239(4):154–65. <https://doi.org/10.1038/scientificamerican1078-154> PMID: 705326
2. Pourquié O. Vertebrate Segmentation: From Cyclic Gene Networks to Scoliosis. *Cell.* 2011; 145(5):650–63. <https://doi.org/10.1016/j.cell.2011.05.011> PMID: 21620133
3. Kefi S, Rietkerk M, Alados CL, Pueyo Y, Papanastasis VP, Elaich A, et al. Spatial vegetation patterns and imminent desertification in Mediterranean arid ecosystems. *Nature.* 2007; 449(7159):213–7. Epub 2007/09/14. <https://doi.org/10.1038/nature06111> PMID: 17851524.
4. Garfinkel A, Tintut Y, Petrusek D, Bostrom K, Demer LL. Pattern formation by vascular mesenchymal cells. *Proc Natl Acad Sci U S A.* 2004; 101(25):9247–50. <https://doi.org/10.1073/pnas.0308436101> PMID: 15197273.
5. Meinhardt H, Gierer A. Pattern formation by local self-activation and lateral inhibition. *BioEssays.* 2000; 22(8):753–60. [https://doi.org/10.1002/1521-1878\(200008\)22:8<753::AID-BIES9>3.0.CO;2-Z](https://doi.org/10.1002/1521-1878(200008)22:8<753::AID-BIES9>3.0.CO;2-Z) PMID: 10918306.
6. Kondo S, Miura T. Reaction-diffusion model as a framework for understanding biological pattern formation. *Science.* 2010; 329(5999):1616–20. <https://doi.org/10.1126/science.1179047> PMID: 20929839.
7. Gomez C, Ozbudak EM, Wunderlich J, Baumann D, Lewis J, Pourquié O. Control of segment number in vertebrate embryos. *Nature.* 2008; 454(7202):335–9. <https://doi.org/10.1038/nature07020> PMID: 18563087.
8. Vasiev BN, Hogeweg P, Panfilov AV. Simulation of Dictyostelium Discoideum aggregation via reaction-diffusion model. *Phys Rev Lett.* 1994; 73(23):3173–6. <https://doi.org/10.1103/PhysRevLett.73.3173> PMID: 10057306
9. Kerr RA, Levine H, Sejnowski TJ, Rappel W-J. Division accuracy in a stochastic model of Min oscillations in Escherichia coli. *Proc Natl Acad Sci USA.* 2006; 103(2):347–52. <https://doi.org/10.1073/pnas.0505825102> PMID: 16387859
10. Kohyama S, Yoshinaga N, Yanagisawa M, Fujiwara K, Doi N. Cell-sized confinement controls generation and stability of a protein wave for spatiotemporal regulation in cells. *eLife.* 2019; 8:e44591. <https://doi.org/10.7554/eLife.44591> PMID: 31358115
11. Ivanov V, Mizuuchi K. Multiple modes of interconverting dynamic pattern formation by bacterial cell division proteins. *Proceedings of the National Academy of Sciences.* 2010; 107(18):8071–8. <https://doi.org/10.1073/pnas.0911036107> PMID: 20212106
12. Cheng X, Ferrell JE. Spontaneous emergence of cell-like organization in Xenopus egg extracts. *Science.* 2019; 366(6465):631–7. <https://doi.org/10.1126/science.aav7793> PMID: 31672897
13. Tyson JJ, Chen KC, Novak B. Sniffers, buzzers, toggles and blinkers: dynamics of regulatory and signaling pathways in the cell. *Curr Opin Cell Biol.* 2003; 15(2):221–31. [https://doi.org/10.1016/s0955-0674\(03\)00017-6](https://doi.org/10.1016/s0955-0674(03)00017-6) PMID: 12648679.

14. Falcke M, Engel H. Pattern formation during the CO oxidation on Pt(110) surfaces under global coupling. *The Journal of Chemical Physics*. 1994; 101(7):6255–63. <https://doi.org/10.1063/1.468379>
15. Falcke M, Engel H, Neufeld M. Cluster formation, standing waves, and stripe patterns in oscillatory active media with local and global coupling. *Phys Rev E*. 1995; 52(1):763–71. <https://doi.org/10.1103/PhysRevE.52.763> PMID: 9963478
16. Vanag VK, Yang L, Dolnik M, Zhabotinsky AM, Epstein IR. Oscillatory cluster patterns in a homogeneous chemical system with global feedback. *Nature*. 2000; 406(6794):389–91. <https://doi.org/10.1038/35019038> PMID: 10935631
17. Kim M, Bertram M, Pollmann M, Oertzen Av, Mikhailov AS, Rotermund HH, et al. Controlling Chemical Turbulence by Global Delayed Feedback: Pattern Formation in Catalytic CO Oxidation on Pt(110). *Science*. 2001; 292(5520):1357–60. <https://doi.org/10.1126/science.1059478> PMID: 11359007
18. Yang L, Dolnik M, Zhabotinsky AM, Epstein IR. Oscillatory clusters in a model of the photosensitive Belousov-Zhabotinsky reaction system with global feedback. *Phys Rev E*. 2000; 62(5):6414–20. <https://doi.org/10.1103/PhysRevE.62.6414> PMID: 11101977
19. Bertram M, Mikhailov AS. Pattern formation in a surface chemical reaction with global delayed feedback. *Phys Rev E*. 2001; 63(6):066102. <https://doi.org/10.1103/PhysRevE.63.066102> PMID: 11415168
20. Berridge MJ, Lipp P, Bootman MD. The versatility and universality of calcium signalling. *Nat Rev Mol Cell Biol*. 2000; 1(1):11–21. <https://doi.org/10.1038/35036035> PMID: 11413485.
21. Bers DM. Cardiac excitation-contraction coupling. *Nature*. 2002; 415(6868):198–205. <https://doi.org/10.1038/415198a> PMID: 11805843
22. Lechleiter J, Girard S, Peralta E, Clapham D. Spiral calcium wave propagation and annihilation in *Xenopus laevis* oocytes. *Science*. 1991; 252(5002):123–6. <https://doi.org/10.1126/science.2011747> PMID: 2011747.
23. Cheng H, Lederer WJ. Calcium Sparks. *Physiol Rev*. 2008; 88(4):1491–545. <https://doi.org/10.1152/physrev.00030.2007> PMID: 18923188
24. Falcke M. Reading the patterns in living cells—the physics of  $Ca^{2+}$  signaling. *Advances in Physics*. 2004; 53(3):255–440. <https://doi.org/10.1080/00018730410001703159>
25. Shuai JW, Jung P. Optimal ion channel clustering for intracellular calcium signaling. *Proc Natl Acad Sci U S A*. 2003; 100(2):506–10. <https://doi.org/10.1073/pnas.0236032100> PMID: 12518049.
26. Nivala M, Ko CY, Nivala M, Weiss JN, Qu Z. Criticality in intracellular calcium signaling in cardiac myocytes. *Biophys J*. 2012; 102(11):2433–42. Epub 2012/06/21. S0006-3495(12)00520-6 [pii]. <https://doi.org/10.1016/j.bpj.2012.05.001> PMID: 22713558; PubMed Central PMCID: PMC3368125.
27. Sobie EA, Dilly KW, dos Santos Cruz J, Lederer WJ, Jafri MS. Termination of cardiac  $Ca^{2+}$  sparks: an investigative mathematical model of calcium-induced calcium release. *Biophys J*. 2002; 83(1):59–78. [https://doi.org/10.1016/s0006-3495\(02\)75149-7](https://doi.org/10.1016/s0006-3495(02)75149-7) PMID: 12080100
28. Stern MD, Rios E, Maltsev VA. Life and death of a cardiac calcium spark. *J Gen Physiol*. 2013; 142(3):257–74. <https://doi.org/10.1085/jgp.201311034> PMID: 23980195; PubMed Central PMCID: PMC3753601.
29. Song Z, Karma A, Weiss JN, Qu Z. Long-Lasting Sparks: Multi-Metastability and Release Competition in the Calcium Release Unit Network. *PLoS Comput Biol*. 2016; 12(1):e1004671. <https://doi.org/10.1371/journal.pcbi.1004671> PubMed Central PMCID: PMC4701461. PMID: 26730593
30. Roome CJ, Kuhn B. Simultaneous dendritic voltage and calcium imaging and somatic recording from Purkinje neurons in awake mice. *Nature communications*. 2018; 9(1):3388. <https://doi.org/10.1038/s41467-018-05900-3> PMID: 30139936
31. Kockskamper J, Blatter LA. Subcellular  $Ca^{2+}$  alternans represents a novel mechanism for the generation of arrhythmogenic  $Ca^{2+}$  waves in cat atrial myocytes. *J Physiol*. 2002; 545(Pt 1):65–79. <https://doi.org/10.1113/jphysiol.2002.025502> PMID: 12433950.
32. Diaz ME, Eisner DA, O'Neill SC. Depressed ryanodine receptor activity increases variability and duration of the systolic  $Ca^{2+}$  transient in rat ventricular myocytes. *Circ Res*. 2002; 91(7):585–93. <https://doi.org/10.1161/01.res.0000035527.53514.c2> PMID: 12364386
33. Gaeta SA, Bub G, Abbott GW, Christini DJ. Dynamical mechanism for subcellular alternans in cardiac myocytes. *Circ Res*. 2009; 105(4):335–42. <https://doi.org/10.1161/CIRCRESAHA.109.197590> PMID: 19628792.
34. Kohl P, Ravens U. Cardiac mechano-electric feedback: past, present, and prospect. *Prog Biophys Mol Biol*. 2003; 82(1–3):3–9. [https://doi.org/10.1016/s0079-6107\(03\)00022-1](https://doi.org/10.1016/s0079-6107(03)00022-1) PMID: 12732264.
35. ter Keurs HE, Wakayama Y, Sugai Y, Price G, Kagaya Y, Boyden PA, et al. Role of sarcomere mechanics and  $Ca^{2+}$  overload in  $Ca^{2+}$  waves and arrhythmias in rat cardiac muscle. *Ann N Y Acad Sci*. 2006; 1080:248–67. <https://doi.org/10.1196/annals.1380.020> PMID: 17132788.

36. Iribe G, Ward CW, Camelliti P, Bollensdorff C, Mason F, Burton RA, et al. Axial stretch of rat single ventricular cardiomyocytes causes an acute and transient increase in Ca<sup>2+</sup> spark rate. *Circ Res*. 2009; 104(6):787–95. <https://doi.org/10.1161/CIRCRESAHA.108.193334> PMID: 19197074.
37. Pastore JM, Girouard SD, Laurita KR, Akar FG, Rosenbaum DS. Mechanism linking T-wave alternans to the genesis of cardiac fibrillation. *Circulation*. 1999; 99(10):1385–94. <https://doi.org/10.1161/01.cir.99.10.1385> PMID: 10077525
38. Qu Z, Garfinkel A, Chen PS, Weiss JN. Mechanisms of discordant alternans and induction of reentry in simulated cardiac tissue. *Circulation*. 2000; 102(14):1664–70. <https://doi.org/10.1161/01.cir.102.14.1664> PMID: 11015345
39. Batista CAS, Lopes SR, Viana RL, Batista AM. Delayed feedback control of bursting synchronization in a scale-free neuronal network. *Neural Networks*. 2010; 23(1):114–24. <https://doi.org/10.1016/j.neunet.2009.08.005> PMID: 19726157
40. Rusin CG, Johnson SE, Kapur J, Hudson JL. Engineering the synchronization of neuron action potentials using global time-delayed feedback stimulation. *Phys Rev E*. 2011; 84(6):066202. <https://doi.org/10.1103/PhysRevE.84.066202> PMID: 22304173
41. Huang S, Zhang J, Wang M, Hu C-K. Firing patterns transition and desynchronization induced by time delay in neural networks. *Physica A: Statistical Mechanics and its Applications*. 2018; 499:88–97. <https://doi.org/10.1016/j.physa.2018.01.039>.
42. Golomb D, Rinzel J. Clustering in globally coupled inhibitory neurons. *Physica D: Nonlinear Phenomena*. 1994; 72(3):259–82. [https://doi.org/10.1016/0167-2789\(94\)90214-3](https://doi.org/10.1016/0167-2789(94)90214-3).
43. Song Z, Ko C Y, Nivala M, Weiss James N, Qu Z. Calcium-Voltage Coupling in the Genesis of Early and Delayed Afterdepolarizations in Cardiac Myocytes. *Biophys J*. 2015; 108(8):1908–21. PubMed Central PMCID: PMC4407256. <https://doi.org/10.1016/j.bpj.2015.03.011> PMID: 25902431
44. Song Z, Liu MB, Qu Z. Transverse tubular network structures in the genesis of intracellular calcium alternans and triggered activity in cardiac cells. *J Mol Cell Cardiol*. 2018; 114:288–99. <https://doi.org/10.1016/j.yjmcc.2017.12.003> PMID: 29217432
45. Song Z, Qu Z, Karma A. Stochastic initiation and termination of calcium-mediated triggered activity in cardiac myocytes. *Proceedings of the National Academy of Sciences*. 2017; 114(3):E270–E9. <https://doi.org/10.1073/pnas.1614051114> PubMed Central PMCID: PMC5255629. PMID: 28049836
46. Shiferaw Y, Sato D, Karma A. Coupled dynamics of voltage and calcium in paced cardiac cells. *Phys Rev E*. 2005; 71(2 Pt 1):021903. <https://doi.org/10.1103/PhysRevE.71.021903> PMID: 15783348.
47. Qu Z, Shiferaw Y, Weiss JN. Nonlinear dynamics of cardiac excitation-contraction coupling: an iterated map study. *Phys Rev E*. 2007; 75(1 Pt 1):011927. PMID: 17358204.
48. Restrepo JG, Karma A. Spatiotemporal intracellular calcium dynamics during cardiac alternans. *Chaos*. 2009; 19(3):037115. <https://doi.org/10.1063/1.3207835> PMID: 19792040.
49. Wan X, Cutler M, Song Z, Karma A, Matsuda T, Baba A, et al. New experimental evidence for mechanism of arrhythmogenic membrane potential alternans based on balance of electrogenic INCX/ICa currents. *Heart Rhythm*. 2012; 9(10):1698–705. <https://doi.org/10.1016/j.hrthm.2012.06.031> PMID: 22721857
50. Luo CH, Rudy Y. A dynamical model of the cardiac ventricular action potential: I. simulations of ionic currents and concentration changes. *Circ Res*. 1994; 74(6):1071–96. <https://doi.org/10.1161/01.res.74.6.1071> PMID: 7514509
51. Tuteja D, Xu D, Timofeyev V, Lu L, Sharma D, Zhang Z, et al. Differential expression of small-conductance Ca<sup>2+</sup>-activated K<sup>+</sup> channels SK1, SK2, and SK3 in mouse atrial and ventricular myocytes. *American Journal of Physiology—Heart and Circulatory Physiology*. 2005; 289(6 58–6):H2714–H23. <https://doi.org/10.1152/ajpheart.00534.2005> PMID: 16055520
52. Chua SK, Chang PC, Maruyama M, Turker I, Shinohara T, Shen MJ, et al. Small-conductance calcium-activated potassium channel and recurrent ventricular fibrillation in failing rabbit ventricles. *Circ Res*. 2011; 108(8):971–9. Epub 2011/02/26. CIRCRESAHA.110.238386 [pii]. <https://doi.org/10.1161/CIRCRESAHA.110.238386> PMID: 21350217; PubMed Central PMCID: PMC3086382.
53. Hamilton S, Polina I, Terentyeva R, Bronk P, Kim TY, Roder K, et al. PKA phosphorylation underlies functional recruitment of sarcolemmal SK2 channels in ventricular myocytes from hypertrophic hearts. *The Journal of Physiology*. 2019; 0(0). <https://doi.org/10.1113/jp277618> PMID: 30771223
54. Kaneko K. Overview of coupled map lattices. *Chaos*. 1992; 2(3):279–82. <https://doi.org/10.1063/1.165869> PMID: 12779975.
55. Qu Z, Hu G, Ma B, Tian G. Spatiotemporally periodic patterns in symmetrically coupled map lattices. *Phys Rev E*. 1994; 50(1):163–70.
56. Wang S, Xie Y, Qu Z. Coupled iterated map models of action potential dynamics in a one-dimensional cable of coupled cardiac cells. *New Journal of Physics*. 2007; 10:055001.

57. Qu Z, Liu MB, Nivala M. A unified theory of calcium alternans in ventricular myocytes. *Scientific reports*. 2016; 6:35625. <https://doi.org/10.1038/srep35625> PMID: 27762397
58. Karma A, Gilmour RF. Nonlinear dynamics of heart rhythm disorders. *Physics Today*. 2007; 60(3):51–7.
59. Xie LH, Weiss JN. Arrhythmogenic consequences of intracellular calcium waves. *Am J Physiol Heart Circ Physiol*. 2009; 297(3):H997–H1002. <https://doi.org/10.1152/ajpheart.00390.2009> PMID: 19561309; PubMed Central PMCID: PMC2755983.
60. Shiferaw Y, Karma A. Turing instability mediated by voltage and calcium diffusion in paced cardiac cells. *Proc Natl Acad Sci U S A*. 2006; 103(15):5670–5. <https://doi.org/10.1073/pnas.0511061103> PMID: 16574775.
61. Aistrup GL, Shiferaw Y, Kapur S, Kadish AH, Wasserstrom JA. Mechanisms underlying the formation and dynamics of subcellular calcium alternans in the intact rat heart. *Circ Res*. 2009; 104(5):639–49. <https://doi.org/10.1161/CIRCRESAHA.108.181909> PMID: 19150887.
62. Mironov S, Jalife J, Tolkacheva EG. Role of Conduction Velocity Restitution and Short-Term Memory in the Development of Action Potential Duration Alternans in Isolated Rabbit Hearts. *Circulation*. 2008; 118(1):17–25. <https://doi.org/10.1161/CIRCULATIONAHA.107.737254> PMID: 18559701
63. Gizzi A, Cherry EM, Gilmour RF Jr., Luther S, Filippi S, Fenton FH. Effects of pacing site and stimulation history on alternans dynamics and the development of complex spatiotemporal patterns in cardiac tissue. *Front Physiol*. 2013; 4:71. <https://doi.org/10.3389/fphys.2013.00071> PMID: 23637684; PubMed Central PMCID: PMC3630331.
64. Lau E, Kossidas K, Kim TY, Kunitomo Y, Ziv O, Song Z, et al. Spatially Discordant Alternans and Arrhythmias in Tachypacing-Induced Cardiac Myopathy in Transgenic LQT1 Rabbits: The Importance of I<sub>Ks</sub> and Ca<sup>2+</sup> Cycling. *PLoS ONE*. 2015; 10(5):e0122754. <https://doi.org/10.1371/journal.pone.0122754> PMID: 25970695
65. Echebarria B, Karma A. Instability and spatiotemporal dynamics of alternans in paced cardiac tissue. *Phys Rev Lett*. 2002; 88(20):208101. <https://doi.org/10.1103/PhysRevLett.88.208101> PMID: 12005608
66. Huang C, Song Z, Landaw J, Qu Z. Spatially Discordant Repolarization Alternans in the Absence of Conduction Velocity Restitution. *Biophys J*. 2020; 118:2574–87. <https://doi.org/10.1016/j.bpj.2020.02.008> PMID: 32101718
67. Panfilov AV, Keldermann RH, Nash MP. Self-Organized Pacemakers in a Coupled Reaction-Diffusion-Mechanics System. *Phys Rev Lett*. 2005; 95(25):258104. <https://doi.org/10.1103/PhysRevLett.95.258104> PMID: 16384515
68. Keldermann RH, Nash MP, Panfilov AV. Modeling cardiac mechano-electrical feedback using reaction-diffusion-mechanics systems. *Physica D: Nonlinear Phenomena*. 2009; 238(11):1000–7. <https://doi.org/10.1016/j.physd.2008.08.017>.
69. Weise LD, Panfilov AV. Mechanism for Mechanical Wave Break in the Heart Muscle. *Phys Rev Lett*. 2017; 119(10):108101. <https://doi.org/10.1103/PhysRevLett.119.108101> PMID: 28949179
70. Precht JC, Cohen LB, Pesaran B, Mitra PP, Kleinfeld D. Visual stimuli induce waves of electrical activity in turtle cortex. *Proc Natl Acad Sci U S A*. 1997; 94(14):7621–6. <https://doi.org/10.1073/pnas.94.14.7621> PMID: 9207142.
71. Huang X, Troy WC, Yang Q, Ma H, Laing CR, Schiff SJ, et al. Spiral waves in disinhibited mammalian neocortex. *J Neurosci*. 2004; 24(44):9897–902. <https://doi.org/10.1523/JNEUROSCI.2705-04.2004> PMID: 15525774.
72. Schiff SJ, Huang X, Wu JY. Dynamical evolution of spatiotemporal patterns in mammalian middle cortex. *Phys Rev Lett*. 2007; 98(17):178102. <https://doi.org/10.1103/PhysRevLett.98.178102> PMID: 17501537.
73. Dombeck DA, Graziano MS, Tank DW. Functional Clustering of Neurons in Motor Cortex Determined by Cellular Resolution Imaging in Awake Behaving Mice. *The Journal of Neuroscience*. 2009; 29(44):13751–60. <https://doi.org/10.1523/JNEUROSCI.2985-09.2009> PMID: 19889987
74. Restrepo JG, Weiss JN, Karma A. Calsequestrin-mediated mechanism for cellular calcium transient alternans. *Biophys J*. 2008; 95(8):3767–89. <https://doi.org/10.1529/biophysj.108.130419> PMID: 18676655; PubMed Central PMCID: PMC2553104.
75. Tao T, O'Neill SC, Diaz ME, Li YT, Eisner DA, Zhang H. Alternans of cardiac calcium cycling in a cluster of ryanodine receptors: a simulation study. *Am J Physiol Heart Circ Physiol*. 2008; 295(2):H598–609. <https://doi.org/10.1152/ajpheart.01086.2007> PMID: 18515647
76. Rovetti R, Cui X, Garfinkel A, Weiss JN, Qu Z. Spark-Induced Sparks As a Mechanism of Intracellular Calcium Alternans in Cardiac Myocytes. *Circ Res*. 2010; 106:1582–91. <https://doi.org/10.1161/CIRCRESAHA.109.213975> PubMed Central PMCID: PMC2893409. PMID: 20378857

77. Nivala M, de Lange E, Rovetti R, Qu Z. Computational modeling and numerical methods for spatiotemporal calcium cycling in ventricular myocytes. *Front Physiol.* 2012; 3:114. Epub 2012/05/16. <https://doi.org/10.3389/fphys.2012.00114> PMID: 22586402; PubMed Central PMCID: PMC3346978.
78. Colman MA, Pinali C, Trafford AW, Zhang H, Kitmitto A. A computational model of spatio-temporal cardiac intracellular calcium handling with realistic structure and spatial flux distribution from sarcoplasmic reticulum and t-tubule reconstructions. *PLOS Computational Biology.* 2017; 13(8):e1005714. <https://doi.org/10.1371/journal.pcbi.1005714> PMID: 28859079
79. Komendantov AO, Komendantova OG, Johnson SW, Canavier CC. A Modeling Study Suggests Complementary Roles for GABAA and NMDA Receptors and the SK Channel in Regulating the Firing Pattern in Midbrain Dopamine Neurons. *J Neurophysiol.* 2004; 91(1):346–57. <https://doi.org/10.1152/jn.00062.2003> PMID: 13679411.